Towards measuring the Spin-Hall effect in a Bose-Einstein condensate

M.R. Faber
3785041

Supervision: prof. dr. P. van der Straten and P.C. Bons MSc

June 18, 2014

Abstract

This bachelor's thesis is split into three parts. In the first part, we explore the realisability of a light-induced artificial gauge field in a Bose-condensed gas of sodium atoms. We find that it should indeed be possible to implement a setup that should lead to measurable phenomena in a Bose-gas. After that, we investigate the influence of short-circuiting in a magnetic trap for Bose-condensed sodium atoms. Here, we conclude that it is possible to undo the observable changes in the magnetic trap by carefully choosing the current through a set of fine tuning coils. Finally, we develop a pseudo-classical model to compute the spectrum obtained in saturated absorption spectroscopy and apply this to the D2-line in sodium atoms.

Contents

WARNING FOR THE READER

This is an unmarked and uncorrected version of my bachelor's thesis and is hence prone to contain errors. In due time, I will be trying to revise this document. If a revision is not available on Igitur, the reader may contact the author or his supervisor for a revised version.

1 Towards artificial gauge fields in a Bose-gas

In recent years, the field of spintronics has become of great interest to physicists. To achieve the desired spin currents, one can make use of the spin Hall effect where one has a force perpendicular to the velocity of the spins. In neutral atoms, it can be challenging to generate forces perpendicular to the atom's velocity. The problem of generating a force perpendicular to the velocity can be solved in numerous ways, including rotating the atoms so that a Coriolis force and a centrifugal force arise in the atom's frame of reference, corresponding to a vector potential and a electric potential respectively. One of the limitations that come with this solution is the lack of spin-dependence, which means it does not cause a Hall effect.

Here, we investigate how two counter-propagating laser beams can be used to generate an artificial gauge field, similar to a magnetic field that gives rise to a Lorentz force. In a semi-classical picture, the Lorentz force may be seen as arising from a combination of the optical dipole forces and radiation pressure forces to which the atom is subjected in the electromagnetic field of the laser beams [1].

1.1 Theoretical description

Here, we follow the approach set out by *Zhu et al.*[2] and *Korenberg*[3]. By exploiting a Λ-scheme, where two ground states $|1\rangle$ and $|2\rangle$ are coupled through a virtual state below an excited state $|3\rangle$, we can create an artificial gauge field with the same properties as a spatially dependent magnetic field. The Hamiltonian that arises when an atom is subjected to a electromagnetic field, that couples $|1\rangle$ and $|2\rangle$ can be written as

$$\hat{H} = \frac{\hat{\mathbf{p}}^2}{2m} + \hat{V}(\mathbf{r}) + \hbar\hat{U}(\mathbf{r}), \tag{1}$$

for the momentum operator $\hat{\mathbf{p}}$, a potential $V(\mathbf{r})$ and a light coupling term $\hat{U}(\mathbf{r})$. Here, m denotes the mass of the atom and $\hbar$ is the reduced Planck's constant. For the system of our interest, $\hat{U}(\mathbf{r})$ looks like

$$\hat{U}(\mathbf{r}) = \begin{pmatrix} 0 & 0 & \Omega_1 \\ 0 & 0 & \Omega_2 \\ \Omega_1^* & \Omega_2^* & 2\Delta \end{pmatrix}, \tag{2}$$

where we used Ω_i to denote the Rabi frequency from ground state $|i\rangle$ to the excited state $|3\rangle$ and Δ to denote the detuning between the light and the transition frequency to state $|3\rangle$.

The Rabi frequencies can be parametrised by:

$$\Omega_1 = \Omega \sin(\theta) e^{i\phi} \tag{3}$$

$$\Omega_2 = \Omega \cos(\theta), \tag{4}$$

for $\Omega = \sqrt{|\Omega_1|^2 + |\Omega_2|^2}$ and spatially dependent θ and ϕ. For further convenience, we now define γ by $\tan(\gamma) = \frac{\sqrt{\Omega^2+\Delta^2}-\Delta}{\Omega}$. It can then be shown that the eigenstates of $\hat{U}(\mathbf{r})$ are

$$(|\chi_1\rangle, |\chi_2\rangle, |\chi_3\rangle) = \begin{pmatrix} \cos(\theta) & \sin(\theta)\cos(\gamma)e^{i\phi} & \sin(\theta)\sin(\gamma)e^{i\phi} \\ -\sin(\theta)e^{-i\phi} & \cos(\theta)\cos(\gamma) & \cos(\theta)\sin(\gamma) \\ 0 & -\sin(\gamma) & \cos(\gamma) \end{pmatrix}, \tag{5}$$

with corresponding eigenvalues $(\lambda_1, \lambda_2, \lambda_3) = (0, \Delta - \sqrt{\Delta^2 + \Omega^2}, \Delta + \sqrt{\Delta^2 + \Omega^2})$. Then after projecting the Hamiltonian on the $(|\chi_1\rangle, |\chi_2\rangle, |\chi_3\rangle)$-basis, doing a minimal substitution and neglecting the off-diagonal terms by assuming the *adiabatic condition* (which we will discuss later), we may rewrite the Hamiltonian as

$$\hat{H}_{adiab.} = \frac{(\hat{\mathbf{p}} - \tilde{\mathbf{A}}(\mathbf{r}))^2}{2m} + \tilde{V}(\mathbf{r}), \tag{6}$$

for $\tilde{\mathbf{A}}_{jk} = i\hbar \langle\chi_j| \nabla |\chi_k\rangle$ and $\tilde{V} = \sum_{j\neq k} \frac{\tilde{\mathbf{A}}_{jk}\tilde{\mathbf{A}}_{kj}}{2m} + \hat{V} + \hbar\lambda_j$. Now we can write an eigenstate of $\hat{H}$ as:

$$|\mathbf{\Phi}(\mathbf{r})\rangle = \sum_{j=1}^{3} \mathbf{\Psi}_j(\mathbf{r}) |\chi_j(\mathbf{r})\rangle \tag{7}$$

for $\mathbf{\Psi}_j$ obeying $i\hbar\frac{\partial \mathbf{\Psi_j}}{\partial t} = \hat{H}_{adiab.}\mathbf{\Psi}_j$. A known characteristic of this system is the existence of an eigenstate $|\mathbf{\Phi}(\mathbf{r})\rangle$ that contains no contribution from $|\chi_3\rangle$. This is precisely the state in which we are interested, because it allows for the implementation of the Λ-scheme discussed earlier. We shall thus be considering the case where $\mathbf{\Psi}_3$ is negligible.

Notice that equation 6 has the same structure as the Hamiltonian arising from a magnetic field and that the quantity $\hat{\mathbf{F}} = \hat{\mathbf{v}}(\mathbf{r}) \times (\nabla \times \tilde{\mathbf{A}}(\mathbf{r})) + \nabla\tilde{V}(\mathbf{r})$ may be interpreted as a Lorentz force (here $\hat{\mathbf{v}}$ is the velocity operator). By explicit calculation, it can be shown that

$$\mathbf{B} = \pm\hbar\sin(2\theta)(\nabla\theta \times \nabla\phi), \tag{8}$$

where the plus sign occurs for particles in the $|1\rangle$ state and the minus sign occurs for particles in the $|2\rangle$ state.

1.1.1 Generating an artificial gauge field - a theoretical description

Among the suggestions [4] to generate an artificial gauge field as described in the previous section, is the setup where two spatially separated, counter-propagating laser beams overlap with a Bose-Einstein condensate. The lasers can be described by:

$$\Omega_1 = \Omega_0 \exp(\frac{-(y-a)^2 - x^2}{w^2}) \exp(-ikz); \tag{9}$$

$$\Omega_2 = \Omega_0 \exp(\frac{-(y+a)^2 - x^2}{w^2}) \exp(ikz),$$

where Ω_0 is the Rabi frequency, $2a$ is the distance between the lasers, w is the waist and k the wave number. Here, we have chosen the z-axis to coincide with the semi-major axis of the condensate and we have chosen the y-axis in through centre of the condensate, perpendicular to the z-axis and in the direction of the gravitational force. (These conditions also fix the x-axis, in our Cartesian coordinate system.) In the case of a non-negligible external magnetic field, there should be a frequency difference between the lasers to account for the relative shift between the eigenenergies corresponding to $|1\rangle$ and $|2\rangle$.

Since we will be coupling the $|F = 1, m_f = -1\rangle$ ground state with the $|F = 1, m_f = 1\rangle$ ground state of the sodium atom, we will be using circularly polarised light to cause the change in angular momentum.

Using equation 1.2, we can now write down the effective magnetic field experienced by the atoms. For $\phi = 2kz$, the fase difference between the beams, we have

$$\nabla\phi = \begin{pmatrix} 0 \\ 0 \\ 2k \end{pmatrix}$$

while for $\tan(\theta) = \frac{\exp(\frac{-(y-a)^2}{w^2})}{\exp(\frac{-(y+a)^2}{w^2})} = \exp(\frac{4ay}{w^2})$, we have

$$\nabla\theta = \begin{pmatrix} 0 \\ \frac{2a}{w^2}\cosh^{-1}(\frac{4ay}{w^2}) \\ 0 \end{pmatrix}$$

and

$$\sin 2\theta = \cosh^{-1}(\frac{4ay}{w^2}),$$

thus we find

$$\mathbf{B} = \pm\frac{4\hbar ka}{w^2}\begin{pmatrix} \cosh^{-2}(\frac{4ay}{w^2}) \\ 0 \\ 0 \end{pmatrix} \tag{10}$$

As mentioned earlier, we also need to fulfil the adiabatic condition. In [3] it is shown that this is the case whenever

$$\sqrt{\left(\frac{4v_y a}{w^2}\right)^2 + \left(v_z k\right)^2} \ll \alpha\frac{\Omega_0^2}{\Delta}, \tag{11}$$

for v_β the velocity in the β-direction and the adiabatic coefficient α given by:

$$\alpha = \exp(\frac{-2y^2}{w^2})\exp(\frac{-2a^2}{w^2})\cosh^2(\frac{4ay}{w^2}) \tag{12}$$

This presents us with an optimisation challenge. We want

- $\Delta \gg \Omega$, to avoid excitation to higher energy states (which would cause particle loss by spontaneous emission to other ground states);
- Ω to be large, to fulfil the adiabatic condition;
- α to be large for as many values of y as possible;
- B to be large for as many values of y as possible.

Since we will be using a laser that is locked at the transition $F = 2$ ground state to an excited state and we start with atoms in the $F = 1$ ground state, the detuning is fixed at 1.77 GHz. In his thesis, S. Korenberg suggests taking $\Omega = 10^8$ Hz and we will follow his advise. For α and B, the free parameters are w and a, the waist and distance between the laser beams. A reasonable starting point for the choice of these parameters would be $w = 60\mu m$ and $a = 30\mu m$. As shown in the figures 1.1 and 1.2, these parameters produce only slightly spatially varying adiabatic coefficients and magnetic fields.

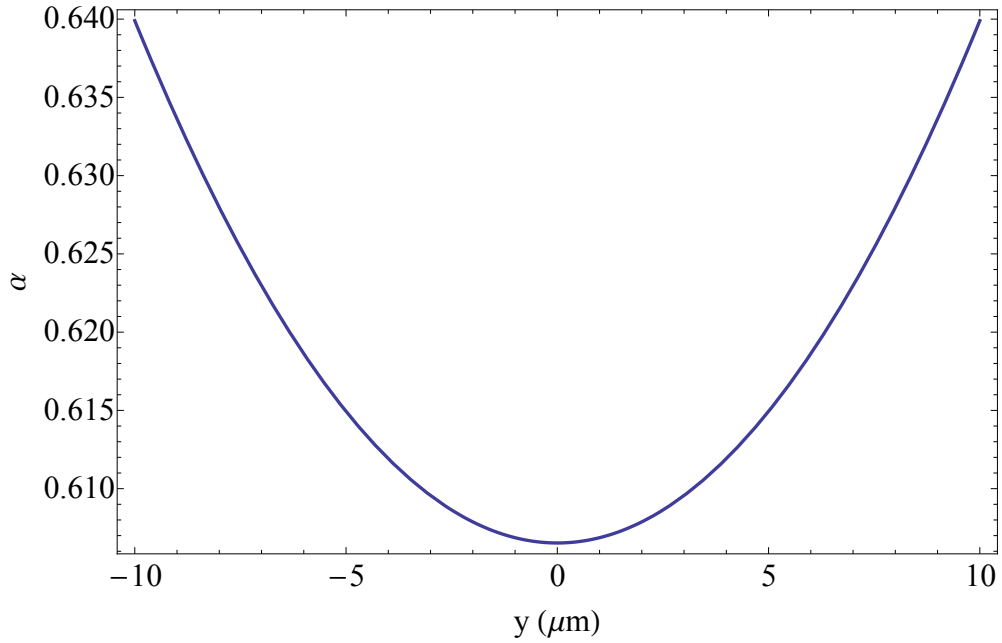

Figure 1.1: *The adiabatic coefficient as a function of y for parameters $w = 60$ μm and $a = 30$ μm.*

1.2 Experimental implementation

To generate the artificial gauge field described earlier, we need a pair of counter-propagating Gaussian beams with the correct geometry. Since the waist $w(z)$ as a function of z (where

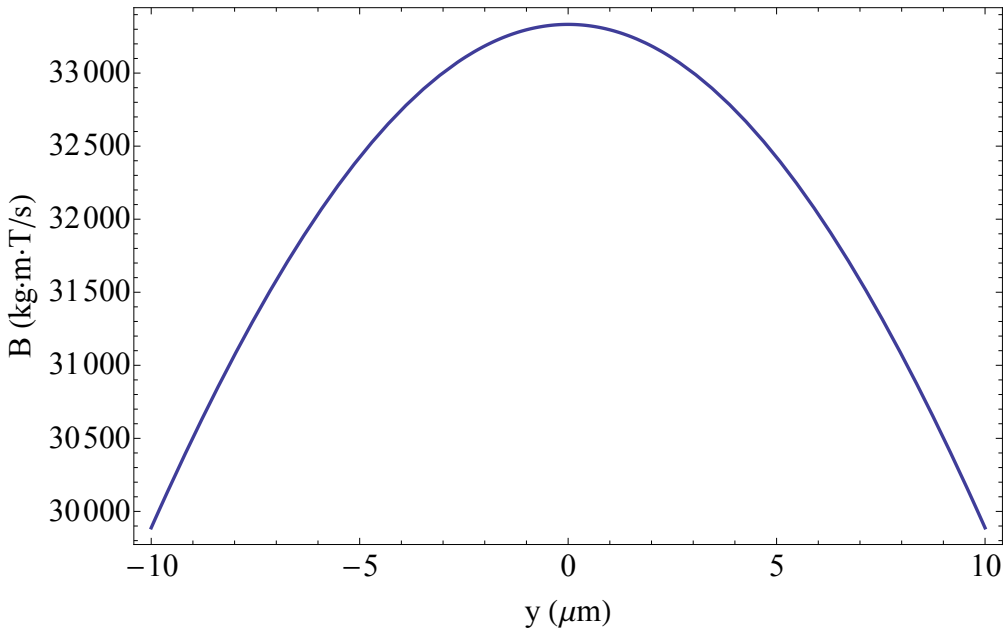

Figure 1.2: *The magnetic field as a function of y in units of $\hbar k$ times the magnetic induction for parameters $w = 60\ \mu m$ and $a = 30\ \mu m$.*

z is the direction of propagation) can be written as

$$w(z) = w_0 \sqrt{1 + \left(\frac{z - z_0}{z_R}\right)^2} \tag{13}$$

for $z_R = \frac{\pi w_0^2}{\lambda}$, the Rayleigh range, and w_0 the minimal value of $w(z)$, which it reaches in $z = z_0$, we can only fix the waist within a desired range for a limited collection of values of z. Typically, one chooses these values of z to be centred around z_0, because the slope of $w(z)$ is also smallest there.

We can tune w_0 and z_0 by choosing a combination of fibre ports and lenses. A fibre port produces a collimated beam with a fixed waist w^* when it comes out of the device. Then, the beam at distance z from the fibre port can be described by the vector:

$$\mathbf{b} = \begin{pmatrix} q \\ 1 \end{pmatrix}, \tag{14}$$

where $\frac{1}{q} = \frac{1}{R} - \frac{i\lambda}{\pi n w^2}$, with index of refraction n, waist w at distance z and radius of curvature R at distance z. If the beam then passes through a lens with focal distance f, $\mathbf{b}$ transforms into:

$$\mathbf{b}' = \begin{pmatrix} 1 & 0 \\ \frac{-1}{f} & 0 \end{pmatrix} \mathbf{b} \tag{15}$$

For different values of f and $w*$, we can then plot the waist of the beam as a function of the distance from the lens. The results can be viewed in figure 1.3. In particular, if we choose $w^* = 1.23$ mm and $f = 0.4$ m or $w^* = 0.92$ mm and $f = 0.3$ m we observe that $w_0 = 66$ μm, which is comparable to the value we are looking for.

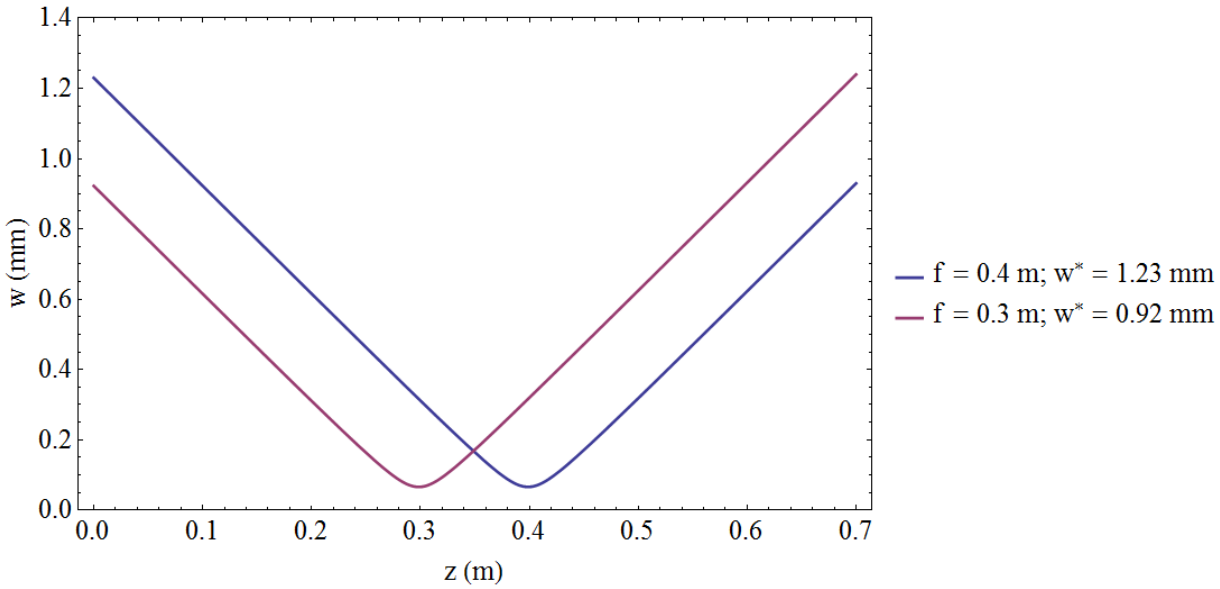

Figure 1.3: *The waist of a Gaussian beam, at a distance z from a lens.*

1.3 Layout of the experiment

For the measurements, we will be using a setup as depicted schematically in the figures 1.4 and 1.5. The numbers correspond to the following components:

1. broadband dielectric mirror (Thorlabs BB1-E02)
2. telescope, magnification 1.5 (lenses Thorlabs LA1257-A and Thorlabs LC1439-A)
3. fiber port (Thorlabs PAF-X-7-A)
4. longpass dichroic mirror (Thorlabs DMLP900 2")
5. precision translation stage for translations in the μm regime (Thorlabs PT1A/M)
6. $f = 30$ cm achromatic lens (Thorlabs AC508-300-B)
7. zero-order $\lambda/4$-waveplate (Thorlabs WPQ05M-588)
8. longpass dichroic mirror (Thorlabs DMLP900 1")
9. translation stage

10. $f = 40$ cm plano-convex lens (Thorlabs LA1172-A)
11. zero-order $\lambda/4$-waveplate (Thorlabs WPQ05M-588)
12. broadband dielectric mirror (Thorlabs BB1-E02)
13. telescope, magnification 2 (lenses Thorlabs LA1251-A and Thorlabs LC1439-A)
14. fiber port (Thorlabs PAF-X-7-A)

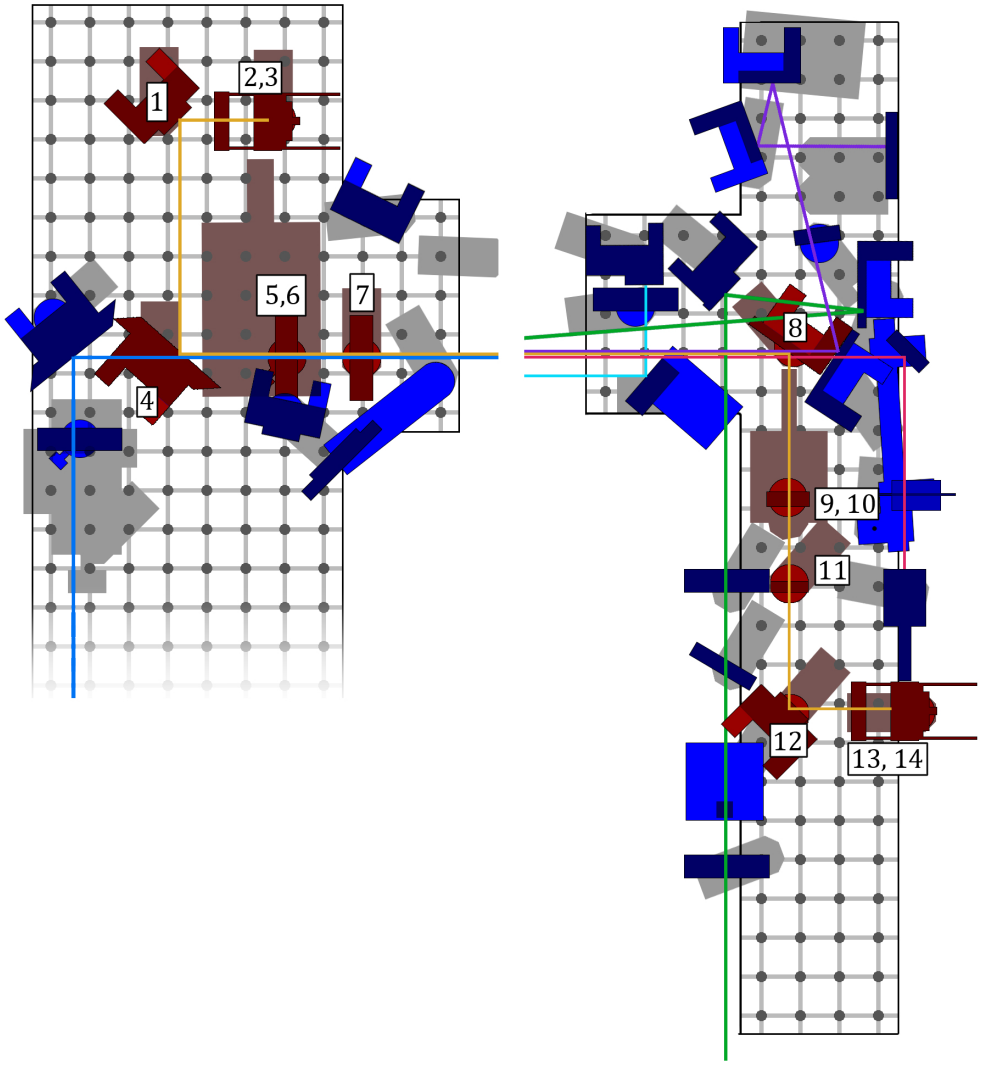

Figure 1.4: *Scaled overview of the optical components in the experiment. The numbered red components are to be added for the generation of the artificial gauge field, whereas the blue components are already part of the Bose-Einstein experiment. See text for an explanation of the numbered components.*

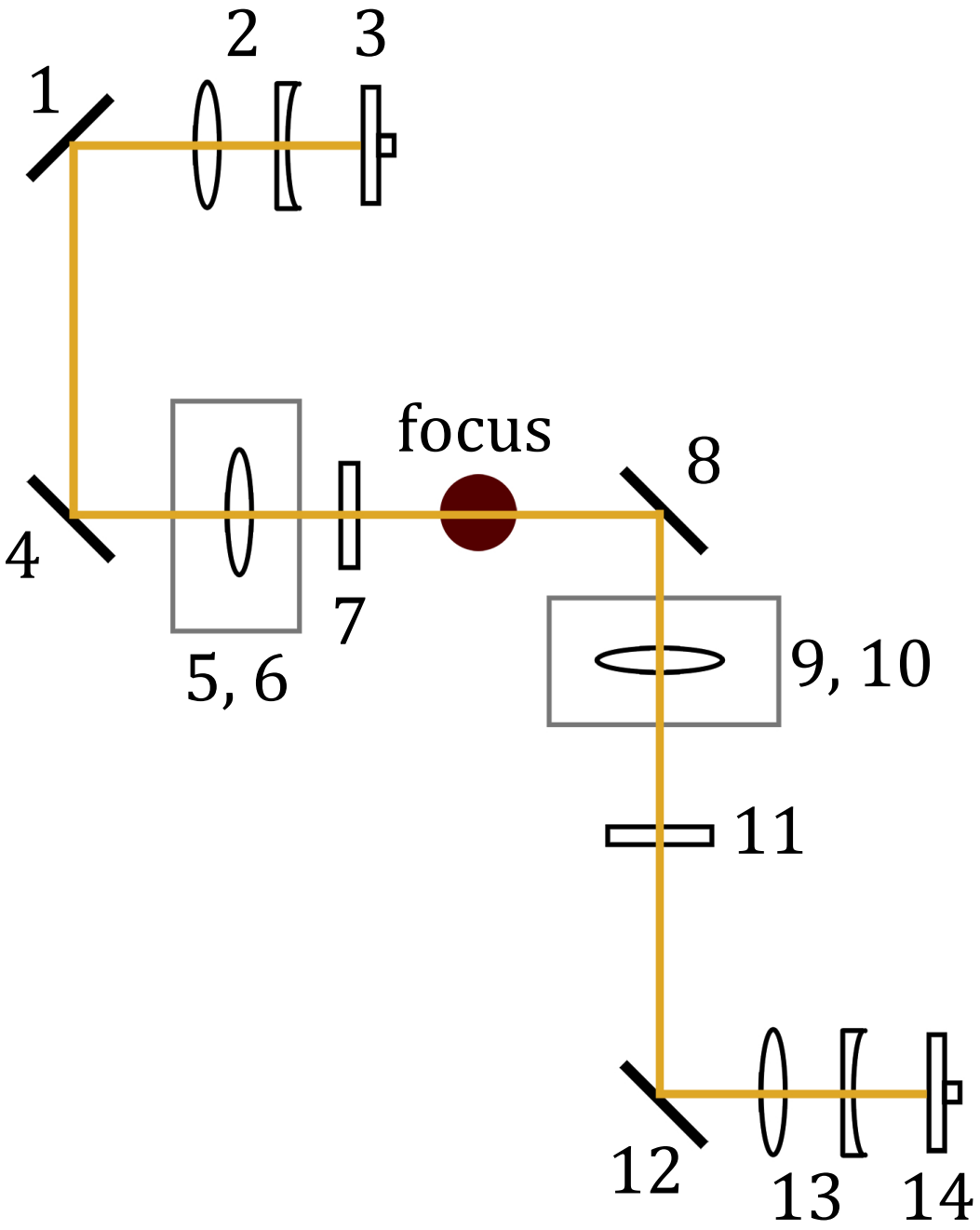

Figure 1.5: *Schematic overview of the artificial gauge field experiment.*

1.3.1 Alignment of the beams

Since both beams need to be propagating exactly anti-parallel at a distance in the order of tens of μm from each other, the alignment of the beams can be challenging. In order to reach the desired accuracy, we must align the beams in steps:

1. Collimate both laser beams out of their respective fibre ports. This can be done by minimizing the spot size of the beams on flat surface at a distance of a few meters from the fibre ports.

2. Place the telescopes in front of the fibre ports and again collimate both beams, this time only adjusting the telescope.

3. Using two of the four mirrors and the lenses (6 and 10), align one beam, such that it couples into a fibre on the other fibre port with maximum power efficiency.

4. Using the other two mirrors, align the other beam, such that it couples into a fibre on the first fibre port with maximum power efficiency.

5. Repeat the last two steps until a maximum power efficiency is reached in both directions, it should now not be necessary to further adjust the lenses.

6. Finally, for a precise alignment of the precision translation stage, measure the power coupled into a fibre as a function of the adjustment of the stage. The result of such a measurement can be viewed in figure 1.6.

This procedure results in a very precise overlap (the distance between the beams is in the order of μm, see figure 1.7 and table 1) of both laser beams, because the fibre ports require alignment with a precision in μm's. After the alignment, the distance between the beams can be tuned at will.

	Waist 1	Δx_0 *1*	*Waist 2*	Δx_0 *2*
Value	$75.5 * 10^{-6}$	$-1.09 * 10^{-4}$	$69.6 * 10^{-6}$	$-1.02 * 10^{-4}$
Uncertainty	$5 * 10^{-7}$	$1 * 10^{-6}$	$5 * 10^{-7}$	$1 * 10^{-6}$

Table 1: *Values of the waist and displacement from the starting position for two knife-edge measurements. The first measurement was of the beam, first propagating through the $f = 0.3$ m lens, and the second measurement was of the beam first propagating through the $f = 0.4$ m lens. The starting position of the knife was the same for both measurements, allowing for the values of Δx_0 to be compared.*

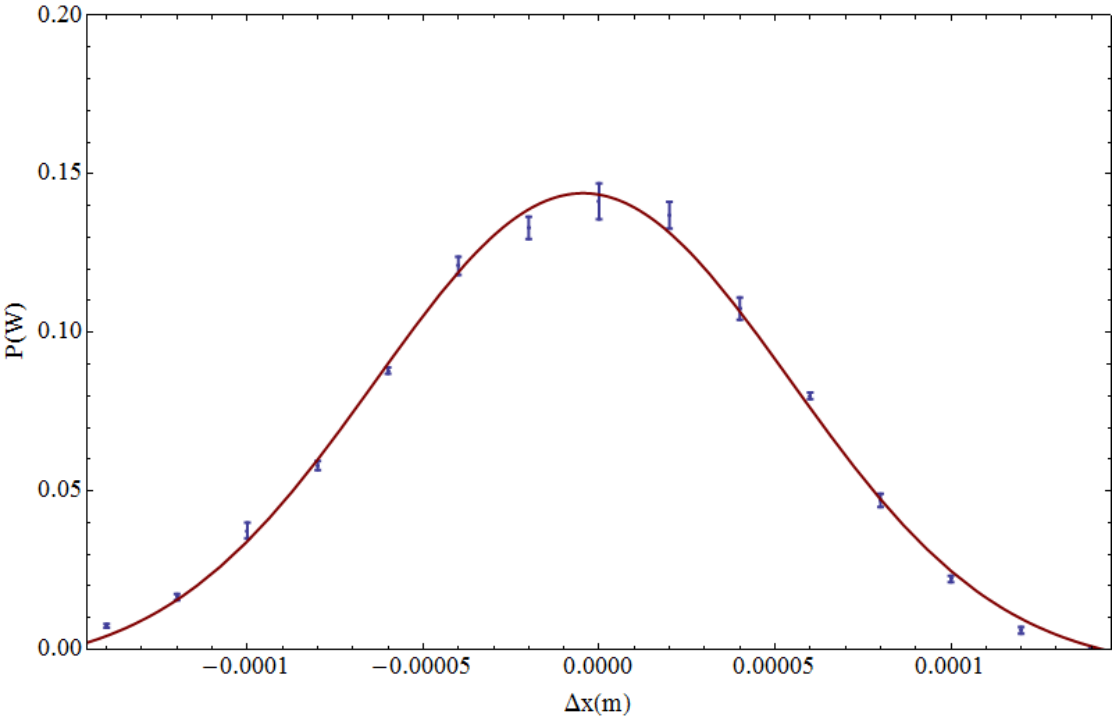

Figure 1.6: *Power coupled into a fibre as a function of the position of the precision translation stage. The red line marks a Gaussian fit through the data points, that showed the power to be maximum for a displacement of* (-4.5 ± 0.9) μm *from the starting position.*

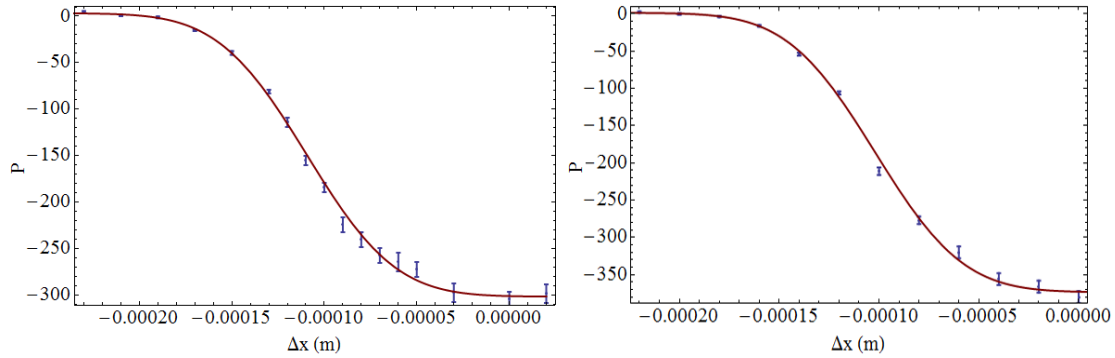

Figure 1.7: *Relative power as a function of the displacement of a knife in a knife-edge measurement of the Gaussian beam profiles. The data are fitted to an error-function that describes the cumulative power. The left plot is of the beam, first propagating through the* $f = 0.3$ *m lens, and the right plot is of the beam first propagating through the* $f = 0.4$ *m lens. For the numerical values of the relevant fitted parameters, see table 1*

1.3.2 Theoretical predictions

Finally, we will do some theoretical predictions for the measurements that are to be done in the future on the suggested scheme. We do this by numerically solving the classical

(semi)-differential equation for two spins that experience an opposite force, due to a spatially varying magnetic field. To this end, we modify the equation as given in [3]:

$$m\begin{pmatrix}\ddot{x}_\uparrow\\ \ddot{y}_\uparrow\\ \ddot{z}_\uparrow\\ \ddot{x}_\downarrow\\ \ddot{y}_\downarrow\\ \ddot{z}_\downarrow\end{pmatrix} = \begin{pmatrix}-\gamma_r & 0 & 0 & \gamma_r & 0 & 0\\ 0 & -\gamma_r & B(y) & 0 & \gamma_r & 0\\ 0 & -B(y) & -\gamma_z & 0 & 0 & \gamma_z\\ \gamma_r & 0 & 0 & -\gamma_r & 0 & 0\\ 0 & \gamma_r & 0 & 0 & -\gamma_r & -B(y)\\ 0 & 0 & \gamma_z & 0 & B(y) & -\gamma_z\end{pmatrix}\begin{pmatrix}\dot{x}_\uparrow\\ \dot{y}_\uparrow\\ \dot{z}_\uparrow\\ \dot{x}_\downarrow\\ \dot{y}_\downarrow\\ \dot{z}_\downarrow\end{pmatrix} + \begin{pmatrix}-m\omega_r^2 & 0 & 0 & 0 & 0 & 0\\ 0 & -m\omega_r^2 & 0 & 0 & 0 & 0\\ 0 & 0 & -m\omega_z^2 & 0 & 0 & 0\\ 0 & 0 & 0 & -m\omega_r^2 & 0 & 0\\ 0 & 0 & 0 & 0 & -m\omega_r^2 & 0\\ 0 & 0 & 0 & 0 & 0 & -m\omega_z^2\end{pmatrix}\begin{pmatrix}x_\uparrow\\ y_\uparrow\\ z_\uparrow\\ x_\downarrow\\ y_\downarrow\\ z_\downarrow\end{pmatrix}. \quad (16)$$

Here, γ_α is the spin-drag [5] coefficient in the α-direction and ω_α is $2\pi f_\alpha$, with f_α the trapping frequency in the α-direction. For $B(y)$, we use equation 10, i.e. $\mathrm{B(y)} = \frac{4\hbar k a}{w^2}\cosh^{-2}(\frac{4ay}{w^2})\hat{e}_x$.

We numerically solve this differential equation for the values as reported in table 2 and for different values of a, ω_r and ω_z. As starting values, we take $x(0) = y(0) = 0$ and $z(0) = 0.1$ mm. This produces the zero-function in the x-direction as the equations of motion in this direction are left completely uncoupled by the equations of motion in the other directions. Next, we numerically Fourier transform the solution and fit it to the analytic Fourier transform of a exponentially dampened sin-function, given by:

$$f(t) = e^{-\alpha t}\sin(\omega t) \quad (17)$$

$$\mathscr{F}(f)(\Omega) = \int_0^{t_{max}} e^{i\Omega t} f(t)dt = \frac{\omega + e^{-t_{max}(\alpha - i\Omega)}(-\omega\cos(t_{max}\omega) - (\alpha - i\Omega)\sin(t_{max}\omega))}{(\alpha - i\omega)^2 + \omega^2}. \quad (18)$$

The results can be viewed in the figures 1.8, 1.9 and 1.10. We observe that for small a, the trapping frequencies converge to ω_z. This can be understood by observing that the axial harmonic term in equation 2.4 becomes dominant for small values of a. This frequency is then also coupled into the y-term, through the magnetic field, resulting in a cyclotron motion, where the frequencies in y- and z-direction are equal. Furthermore, it becomes clear that the influence one can exert on the cyclotron frequencies decreases as the aspect ratio increases.

m (kg)	γ_r (Hz·kg)	γ_z (Hz·kg)	w (μm)	k (nm^{-1})
$0.382 \cdot 10^{-25}$	$100 \cdot m$	$100 \cdot m$	70	$2\pi/589$

Table 2: *Numeric values for the parameters as used in the solution of equation 2.4.*

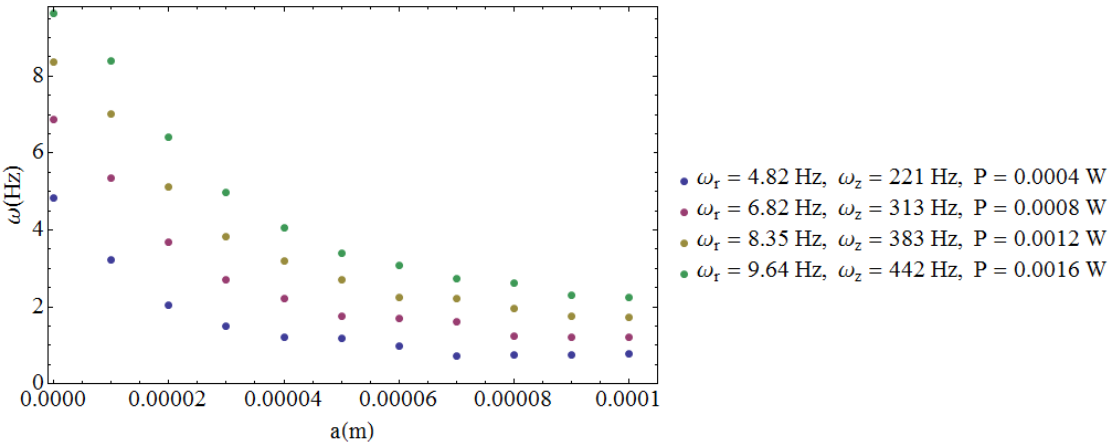

Figure 1.8: *Predicted cyclotron frequency as a function of the distance between the laser beams at aspect ration 45 and waist of the FORT-beam* 10 μm.

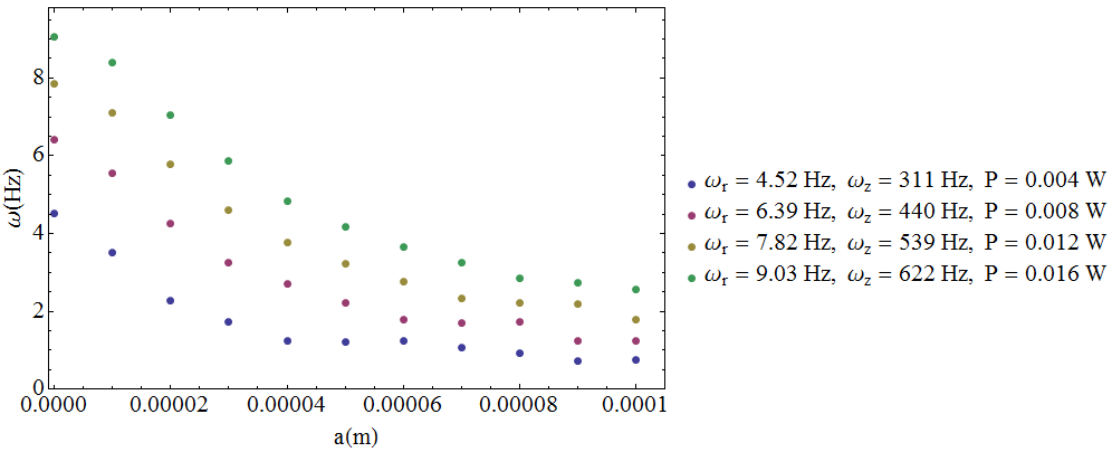

Figure 1.9: *Predicted cyclotron frequency as a function of the distance between the laser beams at aspect ratio 69 and waist of the FORT-beam* 15 μm.

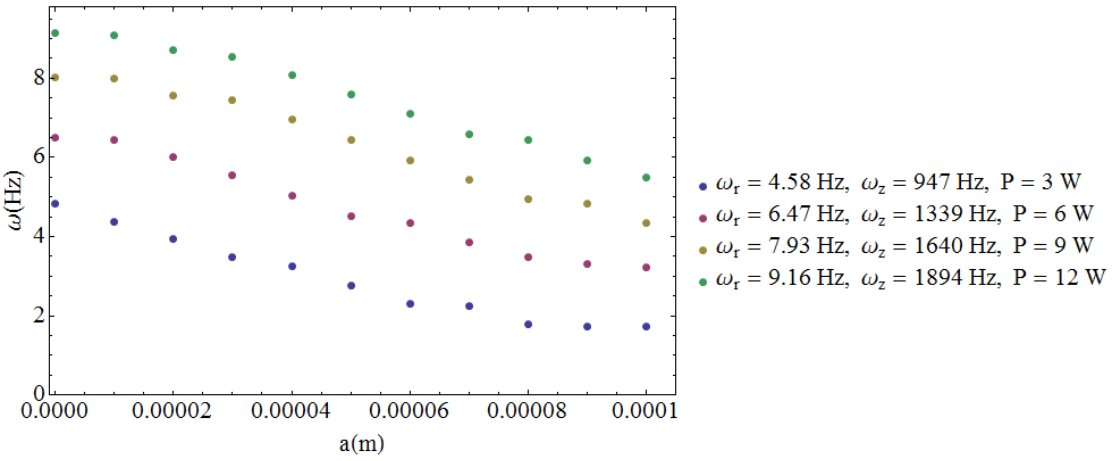

Figure 1.10: *Predicted cyclotron frequency as a function of the distance between the laser beams at aspect ratio 206 and waist of the FORT-beam* 45 μm.

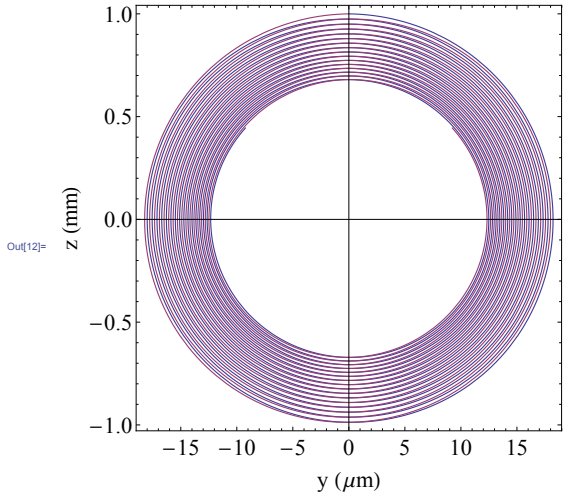

Figure 1.11: *The orbits of both spins, as predicted by the numerical solution of equation 2.4. For this figure, we set* $a = 30$ μm. *Notice the different units on the axes.*

Finally, we investigate the behaviour for large deviations from the origin or large values of a. The resulting Fourier spectrum can be viewed in figure 1.12. We see that the trapping frequency can no longer be well defined, as there is a significant contribution to the Fourier spectrum for different frequencies. This is due to large variation in B on the trajectory of the particle.

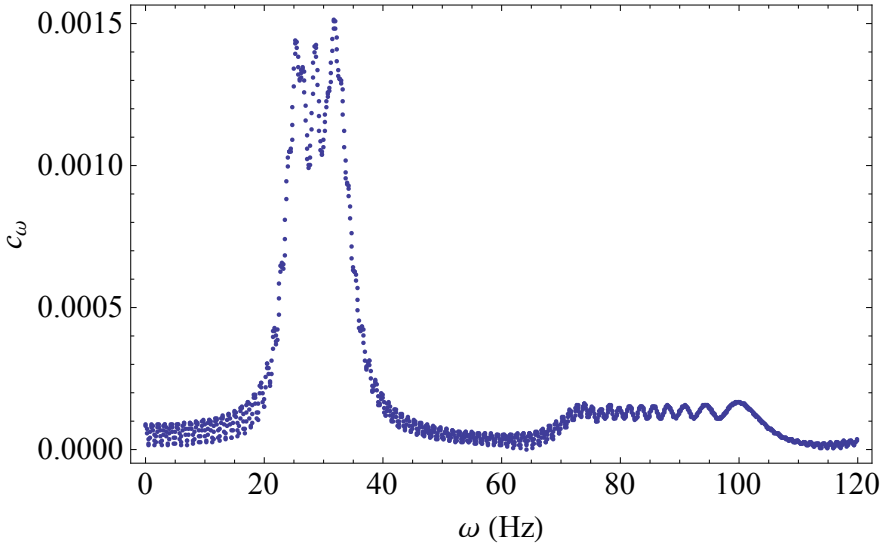

Figure 1.12: *The Fourier spectrum for a large distance between the laser beams ($a = 500$ μm). The adiabatic condition is ignored here.*

1.4 Conclusion

In this chapter, we outlined how a future experiment for generating artificial gauge fields might be realised. We designed an experimental setup that may allow for the research of a spin-Hall effect in a Bose-gas and showed that it is possible to reach alignment of the laser beams within an acceptable accuracy. Furthermore, we simulated the orbits of an atom subjected to the theoretically predicted artificial gauge field, and found a detectable change in the frequency of the cyclotron motion. In doing so, we discovered the impact of the aspect ratio of the FORT on the measured cyclotron frequency: we can exhibit more influence on the frequency in a low aspect ratio.

1.5 Discussion

As a next step towards the realisation of an artificial gauge field, we suggest further investigation on the suggested Λ-scheme. This should serve as an independent proof that it is indeed possible to couple two individual ground states through a virtual eigenstate, making it easier for the final experiment on Bose-condensed atoms to be realised.

Also, we suggest doing the measurements at the lowest aspect ratio attainable, for this should increase the observed effect of the gauge field.

2 Short-circuiting in a magnetic field

2.1 Introduction

To achieve Bose-Einstein condensation in a dilute gas of alkali atoms, one needs to cool the particles down to a temperature in the order of μK. Because it is as yet impossible to reach these temperatures in regular solids, it is necessary for the alkali atoms to avoid any contact with the walls of vacuum chambers, in which a typical experiment with Bose-Einstein condensates is performed. In order to trap the atoms in the centre of a vacuum chamber, a spatially varying magnetic field can be used, because particles with non-zero magnetic moment seek the local extrema of the magnetic field. Particles with positive magnetic moment are trapped in a local maxium, while particles with negative magnetic moment are trapped in a local minimum. Since local maxima are ruled out in the absence of electric currents [6], a magnetic field can only allow for the trapping of atoms with negative magnetic moment.

Producing a suitable magnetic field turns out to be an experimentally challenging task. One of the reasons for this are the large currents (320 A) that are required to generate a significant field. These currents cause heating, which in turn presents us with the necessity to cool the coils. During the past year, we had some heating issues with one of the coils that are used to trap the sodium atoms in our experiment. This led us to disassemble our coil setup, so that we could unclog the cooling channels in the coil in question. After reassembling, the geometry of the magnetic field turned out to have altered slightly: we could still trap the atoms as before, but the trap seemed to have rotated around an angle of about $3\,^\circ$. It was suggested that this change might be caused by short-circuiting in one of the windings. If this were indeed the case, we would need to go through the laborious process of disassembling the trapping setup again. It was therefore suggested that the effects of short-circuiting be calculated first to test this hypothesis. The results of these calculations can be read in this section.

2.2 Description of the magnetic field

In our experiment, we use a combination of coils [7] to produce a harmonic trap. To simulate the magnetic field for the purposes of this section, we incorporate the pinch coils, the bias coils, the fine tuning coils and the cloverleaf/gradient coils. In the experiment, these coils consist of copper wires with a thickness of 3.6 mm, through which runs a cooling channel, except for the fine tuning coils which have a cross-section of 1 mm by 3 mm. The complete setup exhibits reflection symmetry in the $z = 0$ plane and $90\,^\circ$ rotational symmetry around the z-axis. For a more detailed overview, the reader can refer to figure 2.1.
Here, we approximate the setup by a collection of infinitely thin wires and for the cloverleaf coils, we use the extra approximation of circular currents, instead of cloverleaf-shaped ones, in order to avoid the extensive calculation time required to calculate the magnetic field of true cloverleaf coils.

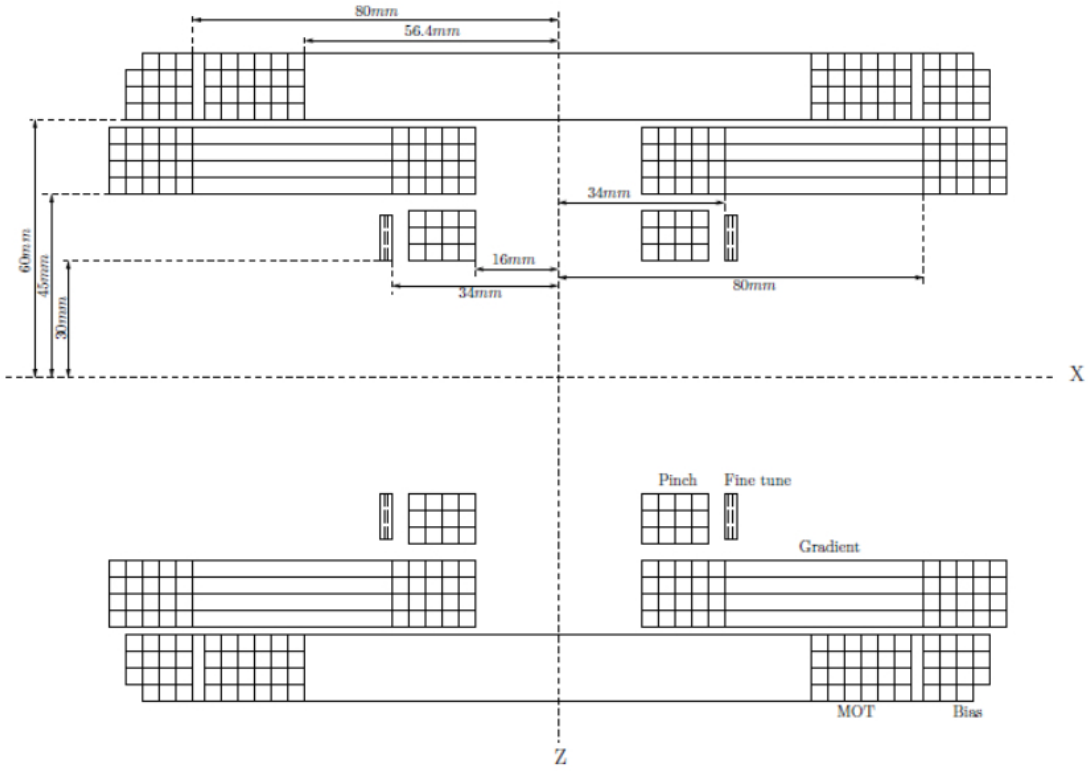

Figure 2.1: *Schematic overview of the magnetic trap. One square corresponds through one wire. The image can be seen as the cross section of the coils and a plane containing the x- or y-axis and the z-axis. Taken from [8].*

The energy shift in a particular quantum state i due to Zeeman Effect, can be written as

$$\Delta E = \mu_B g_F m_F |B| \tag{19}$$

Here, B is the magnetic field and μ_B the Bohr magneton. In the case of the sodium atoms in our experiment, we have $g_F \approx -1/2$ and $m_F = -1$. Since the atoms are in an approximately harmonic trap with $90\,^\circ$ rotational symmetry around the z-axis, this contribution to the energy can be written as

$$\Delta E = \frac{1}{2} m(\omega_z^2 z^2 + \omega_r^2 r^2), \tag{20}$$

where we define ω_z and ω_r to be 2π times the axial and radial trapping frequencies f_z and f_r, respectively.

Furthermore we can approximate the magnetic field by[8]:

$$B_x = B'y - B''xz \tag{21}$$

$$B_y = B'x - B''yz$$

$$B_z = B_0 + B''(z^2 - \frac{x^2+y^2}{2})$$

with

$$B'' = \frac{1}{2}(I_p K_p'' + I_b K_b'') \tag{22}$$

$$B' = I_c K'$$

$$B_0 = I_p K_p + I_b K_b$$

where I_p, I_b and I_c correspond to the currents through the pinch coils, the bias coils and the cloverleaf coils respectively. The value of K_i can be determined experimentally; it can be found in table.

Parameter	*Value*	*Unit*
K_p''	$3.74 * 10^{-3}$	G/A/mm^2
K_b''	$-2.75 * 10^{-4}$	G/A/mm^2
K'	$3.50 * 10^{-2}$	G/A/mm
K_p	1.03	G/A
K_b	-1.02	G/A

Table 3: Experimental values defining the geometry of the trap. These values are taken from[8].

2.2.1 Pinch and bias coils

For confinement along the z-axis, two pairs of coils, called pinch and bias coils are used. The pinch coils are located between ± 30 mm and ± 41.5 mm on the z-axis and consist of four layers of three windings each. The inner radius of these coils is 16 mm and the outer radius is 31.75 mm.

While the pinch coils create the curvature needed for trapping the atoms along the z-axis, they also cause an undesired magnetic field offset. The bias coils serve to compensate for this offset, so the current through the pinch and bias coils run in opposite directions. The bias coils consist of three layers of four windings and one outermost layer of three windings (the winding furthest from the x, y-plane is lacking), making for a total of fifteen windings. These coils are located between $z = 62$ mm and $z = 77.5$ mm with radii ranging from 79.5 mm to 95 mm.

The pinch and bias coils are connected in series. To allow for freedom in the current that flows through both coils, a shunt is used to divert some (up to 125 A) current from the bias coils. The current through pinch and bias coils ranges between 1.6 and 200 A.

2.2.2 Cloverleaf coils

There are a total of eight cloverleaf coils, through which runs a current of up to 320 A each. Four of these coils are located in the $z > 0$-half of the three-dimensional Cartesian coordinate system, while the others are located in the $z < 0$-half. The cloverleaves are oriented in such a way that the direction of each current is opposite to the direction of the currents through the neighbouring cloverleaves (see figure).

Each cloverleaf consists five layers of four windings. The windings form a 'cloverleaf', which consists of a small circular current arc (inner radius 16 mm, total thickness 18 mm) a large current arc (inner radius 80 mm, total thickness 18 mm) and horizontal and vertical line segments connecting both current arcs. One set of four coils is located between $z = 45$ mm and $z = 60.5$ mm, while the other set is located between $z = -45$ mm and $z = -60.5$ mm.

2.2.3 Fine tuning coils

The final set of coils that we will be considering here is the set of fine tuning coils. In order to have the maximum amount of freedom in setting the minimum of the magnetic trap, we use two fine tuning coils. These coils each have two layers of three windings with an innermost radius of 35.5 mm and an outermost radius of 38 mm and are located between $z = \pm 30$ mm and $z = \pm 39.5$ mm. In the experiment, the minimum of the magnetic field is kept fixed at about 4 G, for which a typical current between 1.8 A and 4.8 A through the fine tuning coils is needed. In our simulation, we use slightly higher currents (6.5 A) through the fine tuning coils, because we do not consider contributions such as those from the earth's magnetic field.

2.3 Structure of the notebook

For the calculations in this section, we used a Mathematica notebook. Here, we discuss the structure of the notebook, with the intention that it can be easily used by others in the future.

2.3.1 Elliptic Integrals

Elliptic integrals [9] arise when calculating the arc length of an ellips or doing calculations to solve similar problems. Since the Biot-Savart law involves path integrals, we are confronted with these integrals when considering circular current arcs. In general, an elliptic integral looks like

$$f(x) = \int_c^x R(t, \sqrt{P(t)})dt \tag{23}$$

where R is a rational function and P a polynomial of degree 3 or 4 and c is a constant. In the notebook, we use the so-called *complete elliptic integrals of the first and second kind*. These respectively look like:

$$K(k) = \int_0^1 \frac{dt}{\sqrt{(1-t^2)(1-k^2t^2)}} = \int_0^{\pi/2} \frac{d\theta}{\sqrt{1-k^2\sin^2\theta}} \tag{24}$$

$$E(k) = \int_0^1 \frac{\sqrt{1-k^2t^2}}{\sqrt{1-t^2}}dt = \int_0^{\pi/2} \sqrt{1-k^2\sin^2\theta}d\theta \tag{25}$$

One may find some differences in the notation of these integrals, among those is taking k^2 as the argument instead of k. In our notebook, we use $KK(x)$ to denote $K(x)$ and $EE(x)$ to denote $E(x)$. Furthermore, we use Mathematica's standard methods for calculating these integrals. However, there exist numerous approximations for these integrals that may reduce the calculation time, some of which are provided in the notebook and are there denoted by KKi and EEi (with i an integer). We do not use these here, because our notebook can do the calculations necessary for our purposes in a respectable time.

2.3.2 Magnetic fields

In this section of the notebook, we define the magnetic field of the various components of the magnetic trap. We start with the definition of the magnetic field of a single circular current loop, whose expression in an arbitrary point is readily found in [7]. We convert this to Cartesian coordinates, to avoid complex expressions involving the chain rule when taking derivatives. Here the syntax is $B\gamma 1(i, R, xd, yd, zd, x, y, z)$ for the γ-component of the magnetic field B in the point (x, y, z) of a circular current loop with its centre in (xd, yd, zd), current i and radius R.

Next, we stack several circular current loops to generate the different components of the magnetic field. This results in the functions $Bctot(x, y, z)$, $Bptot(x, y, z)$, $Bbtot(x, y, z)$ and $Bftot(x, y, z)$ for the cloverleaf coils, the pinch coils, the bias coils and the fine tuning coils respectively. The only approximation used in the expression for the last three coils is that of infinitely thin wires, positioned at the centre of the original wires. For the cloverleaf coils, a more drastic approximation is used which is done in multiple steps.

1. Instead of considering each of the twenty windings of one cloverleaf separately, we consider a single winding located at the centre of the original cloverleaf.

2. Next, for simplicity, we replace the leaf-shaped winding by a single current loop, with the same length (i.e. approximately 36.4 mm).

3. Finally, we vary the distance of the current loop with respect to the z-axis (its z-coordinate remains the same as that of the original leaf-shaped winding), so that we obtain the same gradient as observed experimentally (see table 3).

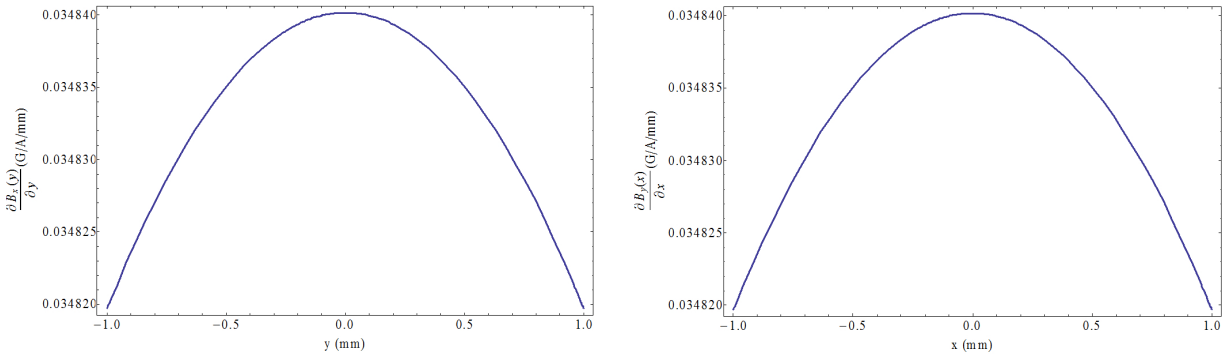

Figure 2.2: *The gradient of the magnetic field as a result of the cloverleaf approximation. Left: the y-derivative of the x-component of the B-field per ampere. Right: the x-derivative of the y-component of the B-field per ampere.*

The resulting gradients can be viewed in figure 2.2 and are in good agreement with the values as in table (3). In figure 2.3 one can view plots of the field by the cloverleaf coils in our approximation, seperated by component as a function of the different coordinates. It behaves as might be expected from equation 21 when there is no contribution from the pinch and bias coils.

2.3.3 Parameters in experiment

This is the section of the notebook in which we define the relevant parameters of the magnetic trap. We used 'i' for the current, 'R' for the radius, 'L' for the total width of the windings and 'x', 'y' and 'z' for the location of the centre of the winding. This is followed by a letter and an index number to denote the type and the number of the coil. Here, we used 'c' for the cloverleaves, 'p' for the pinch coils, 'b' for the bias coils and 'f' for the fine tuning coils. For example, 'Rc3' is the radius of the third cloverleaf coil. In the absence of an index number, the parameter is taken to be the same for every coil of the corresponding type.

Note that the current through the cloverleaf coils is multiplied by 20 to compensate for the reduction of the system 20 of windings, to a single winding. Further note that we used lists for some of the parameters of the pinch, bias and fine tuning coils. The different entries in the lists correspond to different windings on the corresponding coils. Finally note that we defined the current through the fine tuning coils dependent on the pinch and bias coils, so that the final magnetic field has a magnitude of precisely 4 G in the origin. This is done by solving $B_{total}(0,0,0) = 4 * 10^{-4}$ and noting that $B_{total}(0,0,0)$ is completely determined by the contributions from the pinch, bias and fine tuning coils in their axis of rotational symmetry (in which case their expression becomes $\vec{B}(x,y,z) = \vec{B}(z) = \frac{1}{2}\mu_0 I \frac{R^2}{(R^2+z^2)^{3/2}}\hat{e}_3$ for a current I and a radius R), because the contributions of the cloverleaf coils cancel each other in the origin.

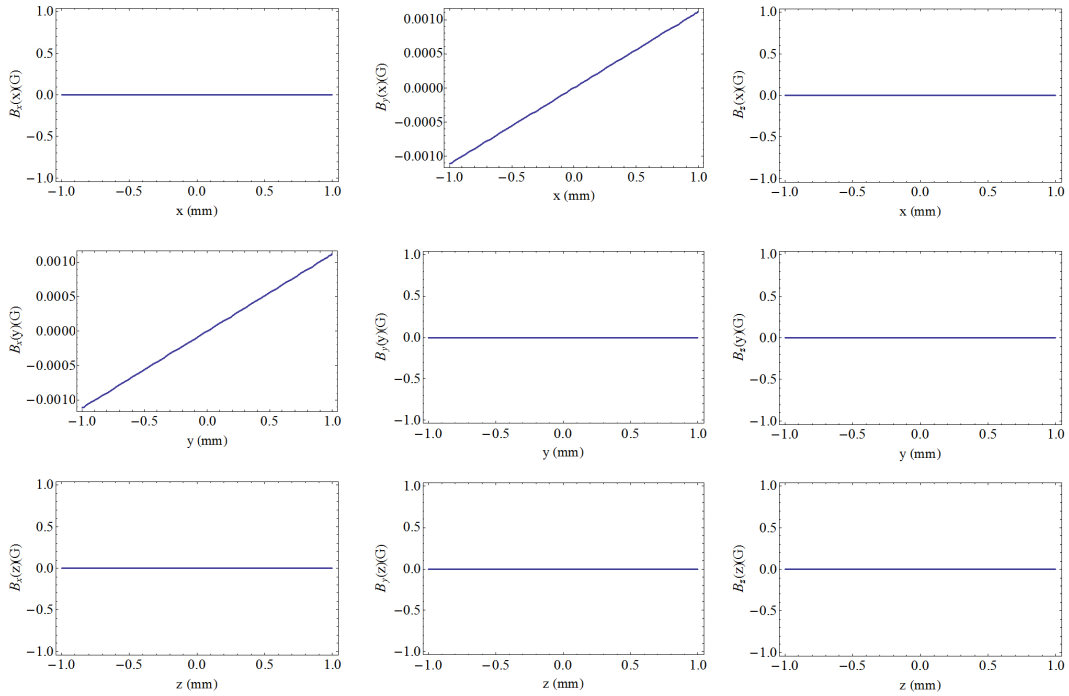

Figure 2.3: *The individual components of the magnetic field from the cloverleaf coils in our approximation. In the left column, we find the x component as a function of x (above), y (centre) and z (below). The centre and right columns are structured the same, with the exception that we plotted the y- and z-components of the field respectively.*

2.3.4 Comparison to experiment

As a test of the performance of our notebook, we compared it with previous work, done by M. van 't Woud[7]. The results can be found in table 4. We observe that we can obtain results for the radial trapping frequencies with approximately the same accuracy as our predecesors, even though we made a drastic approximation to the geometry of the cloverleaf coils. Furthermore, we obtain for the axial trapping frequency a value of 15.5 Hz (this is independent of the current through the cloverleaf coils, for these do not contribute to axial trapping), which is also comparable to the results obtained by Van 't Woud (he found 15.6 Hz).

2.4 Influence of short-circuiting

We now investigate the influence of short-circuiting on the magnetic trap. In figure 2.4, one can observe the absolute value of the magnetic field on the plane $y = 0$. In the normal case, the characteristics of this plot remain the same for every rotation of this plane about the z-axis.
If we short-circuit one of the windings of one of the cloverleaf coils, the total current through the complete coil is decreased by a factor $\frac{19}{20}$, because the are 20 windings in

Current through cloverleaves (A)	Measured f_r (Hz)	Approximated f_r (Hz)	'Exact' f_r (Hz)
320	96.4	97.2	100.8
280	86.2	84.8	88.1
240	76.3	72.5	75.3
200	65.6	60.1	62.4
160	54.0	47.6	49.5
120	49.2	35.0	36.4
80	28.5	21.8	22.8

Table 4: *Comparison of the radial trapping frequency at different currents through the cloverleaf coils to the calculated frequencies as obtained by our notebook and as obtained in [7].*

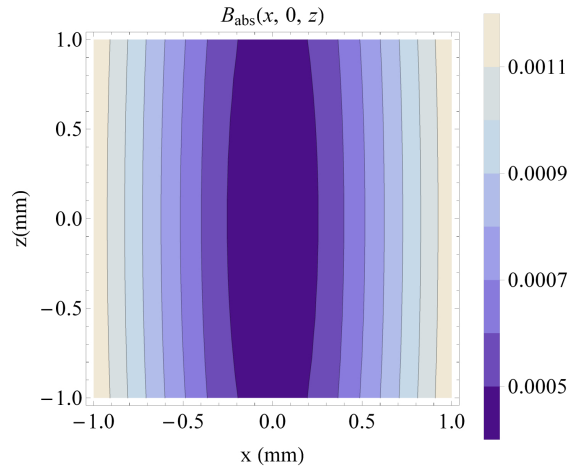

Figure 2.4: *The the absolute value of the magnetic field on the plane $y = 0$ in the normal situation.*

total. In our approximation, we can therefore reduce the current through one of the circular loops that represent the cloverleaf coils by this factor, in order to incorporate this effect. We can then once more plot the absolute value of the field in a plane. This time, however the rotational symmetry in the origin is broken, as can be seen in figures 2.5 and 2.6.

If we want to calculate the new trapping frequency we can then best do this in the new minimum, because the trap is only approximately harmonic. This turns out to be the point

$$(x, y, z) = (0.0002329296794253558, -0.0002329296794253558, 0.00002671424349111232)$$

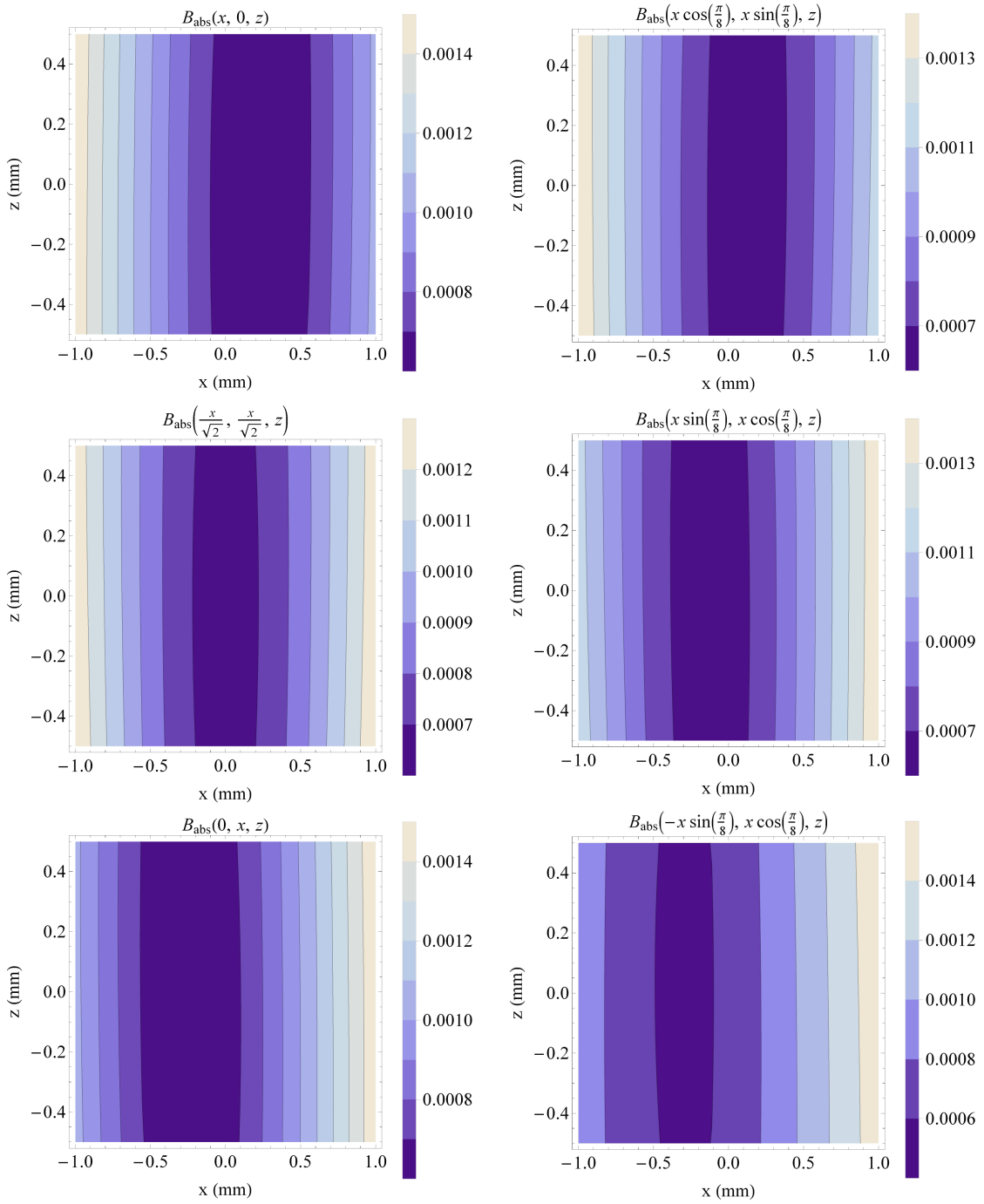

Figure 2.5: *The the absolute value of the magnetic field on different planes through the origin (part 1).*

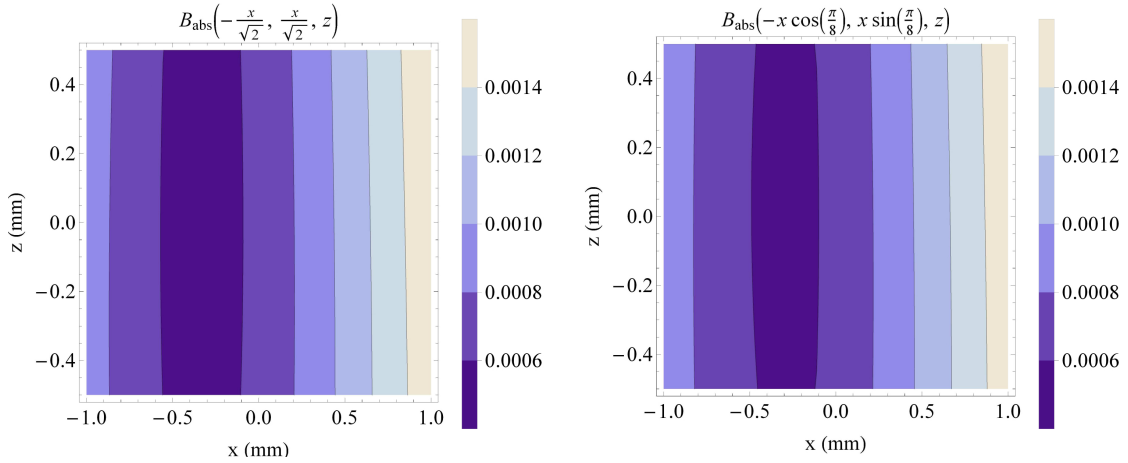

Figure 2.6: *The the absolute value of the magnetic field on different planes through the origin (part 2).*

(the accuracy here has to be large, because dependency on the direction of the calculated curvature turns out to be extremely sensitive when a winding in the cloverleaf coils was short-circuited). The second derivatives in the x-, y- and z-directions can be calculated by solving

$$\begin{pmatrix} 1 & 0 & 0 & 0 & 0 & 0 & 0 & 0 & 0 & 0 \\ 1 & dx & 0 & 0 & dx^2 & 0 & 0 & 0 & 0 & 0 \\ 1 & -dx & 0 & 0 & dx^2 & 0 & 0 & 0 & 0 & 0 \\ 1 & 0 & dy & 0 & 0 & dy^2 & 0 & 0 & 0 & 0 \\ 1 & 0 & -dy & 0 & 0 & dy^2 & 0 & 0 & 0 & 0 \\ 1 & 0 & 0 & dz & 0 & 0 & dz^2 & 0 & 0 & 0 \\ 1 & 0 & 0 & -dz & 0 & 0 & dz^2 & 0 & 0 & 0 \\ 1 & dx & dy & 0 & dx^2 & dy^2 & 0 & dxdy & 0 & 0 \\ 1 & dx & 0 & dz & dx^2 & 0 & dz^2 & 0 & dxdz & 0 \\ 1 & 0 & dy & dz & 0 & dy^2 & dz^2 & 0 & 0 & dydz \end{pmatrix} \begin{pmatrix} B_0 \\ B_x \\ B_y \\ B_z \\ B_{xx} \\ B_{yy} \\ B_{zz} \\ B_{xy} \\ B_{xz} \\ B_{yz} \end{pmatrix} = \begin{pmatrix} B(x,y,z) \\ B(x+dx,y,z) \\ B(x-dx,y,z) \\ B(x,y+dy,z) \\ B(x,y-dy,z) \\ B(x,y,z+dz) \\ B(x,y,z-dz) \\ B(x+dx,y+dy,z) \\ B(x+dx,y,z+dz) \\ B(x,y+dy,z+dz) \end{pmatrix}$$

for the B_α's, where $d\alpha$ is taken to be small. This allows us to make a quadratic expansion in (x, y, z) of the absolute value of the magnetic field:

$$B(x,y,z) = B_0 + B_x x + B_y y + B_z z + B_{xx}x^2 + B_{yy}y^2 + B_{zz}z^2 + B_{xy}xy + B_{xz}xz + B_{yz}yz \quad (26)$$

This approach can be generalised, so that we can use it in rotated bases. The resulting

expressions are omitted, due to their length. We are interested in the radial trapping frequency as a function of the direction in which we take the second derivatives. In the normal harmonic trap, the radial trapping frequency is independent of rotations about the z-axis, hence we want to know whether this property changes if we short-circuit the trap. Furthermore, we want to know the influence of the short-circuiting on the actual magnitude of the trapping frequency. The results can be viewed in figure 2.7. At first

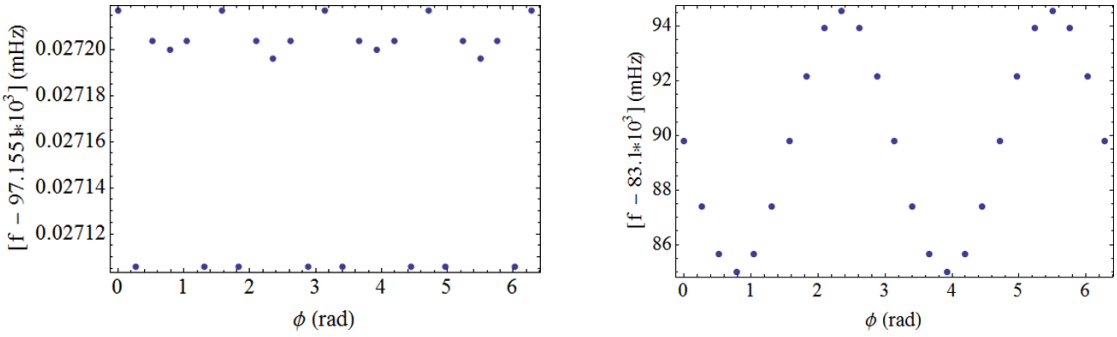

Figure 2.7: Left: *the trapping frequency in the normal case as in the origin. ϕ denotes the angle of rotation of the Cartesian coordinate system about the z-axis.* Right: *the trapping frequency in the short-circuiting case as in the new minimum. ϕ denotes the angle of rotation of the Cartesian coordinate system about the z-axis.*

glance, one might conclude that both the directional dependency and the magnitude of the trapping frequency are altered. However, if we increase the current through the fine tuning coils by approximately 1.6 A, thereby shifting the magnitude of the absolute value of the magnetic field to 4 G, the same as it was in the original case, we can lift the trapping frequency to the old level. Furthermore, if we rotate the coordinate system about the x- and y-axes by an angle of 0.45°, we can reduce the directional dependency. This can be seen in figure 2.8 In all cases, there is no notable change in the axial trapping frequency, as might be expected, since this quantity is mostly determined by the pinch and bias coils.

To investigate the effect of short-circuiting multiple coils, we disabled three extra coils and found a new minimum, namely
$(x, y, z) = (0.0009537805919654539, -0.0009537805919654539, 0.00011629292628640434)$.
Proceding as before, we now had to increase the current through the fine tuning coils by 7.1 A to fix the absolute value of the magnetic field in the minimum at 4 G and rotate the coordinate system about the x- and y-axes by an angle of 0.60°.

2.5 Conclusion

Using an approximation for the cloverleaf coils, we investigated the influence of short-circuiting on the magnetic trap, generated by a collection of coils. We found a change in the location of the minimum of the magnetic field and - initially - of the magnitude

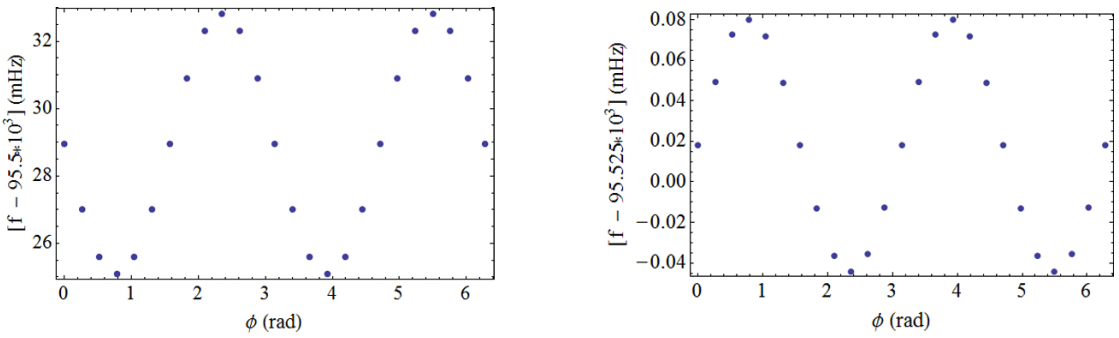

Figure 2.8: Left: *the trapping frequency in the short-circuiting case as in the new minimum. Here the current through the fine tuning coils is increased by* 1.6 *A, whereas the orientation of the axes remains unaltered.* ϕ *denotes the angle of rotation of the Cartesian coordinate system about the z-axis.* Right: *the trapping frequency in the short-circuiting case as in the new minimum. Here both the current through the fine tuning coils and the orientation of the axes are altered.* ϕ *denotes the angle of rotation of the Cartesian coordinate system about the z-axis.*

and the angular dependency of the trapping frequency. However, by altering the current through the fine tuning coils and by rotating our coordinate system, we could nullify the last two changes, thereby constructing a situation closely resembling the original.

The observed translation is realistic in the context of our experiment: the Bose-Einstein condensates are imaged on a camera with a sensor that would register translations in these order as a change in the location of the condensate of a few pixels. During the recalibration of the experiment, a rotation of the condensate by an angle of approximately 3° was reported. This rotation is an order of magnitude larger than the rotation found by our simulation, indicating that short-circuiting cannot be the sole reason for the observed changes in the experiment. This suggests that the rotation might be due to a change in the lay-out of the coils. Because the magnetic field results from the subtraction of strong magnetic fields generated by the individual coils, the system is sensitive to small changes in the exact location of the coils, thereby making it hard to judge from simulation alone what is the cause for these changes.

Finally, when we short-circuited four coils, we found an unrealistically large increase in the current through fine tuning coils to be necessary to again fix the value of the minimum at 4 G. Even in this extreme scenario, we were unable to reconstruct the angle of rotation that was originally reported.

2.6 Discussion

For a definite answer to the question as of what causes the magnetic field to rotate by an angle of approximately 3°, manual inspection of the magnetic coils in necessary.

However, since this task is laborious by nature, we suggest this be only carried, when serious concerns about damage to the coils by short-circuiting arise. The current state of the magnetic coils allows for the trapping of Bose-Einstein condensates, and thus the coils fulfil their original purpose, obscuring the need for further extensive investigations.

3 Saturated absorption spectroscopy

In this section, we shall give a theoretical description of the saturated absorption spectroscopy of a system with n ground-level states and a first excited state with m-fold hyperfine splitting. We do this by generalising the two-level system, described in [10], to the larger type of system of our interest.

Let $|g_1\rangle, |g_2\rangle, ..., |g_n\rangle$ be the ground states of an atom with energies $E_{g_1}, E_{g_2}, ..., E_{g_n}$ and let $|e_1\rangle, |e_2\rangle, ..., |e_m\rangle$ be the excited states with energies $E_{g_1}, E_{g_2}, ..., E_{g_n}$. We denote the transition frequency between the states $|g_i\rangle$ and $|e_j\rangle$ by ν_{ij}.

There are three transition processes involved in saturated absorption spectroscopy, namely:

1. *Stimulated absorption* of a photon by an atom in a ground state $|g_i\rangle$, which causes the atom to transfer to an excited state $|e_j\rangle$.

2. *Stimulated emission* by a photon of an atom in an excited state $|e_j\rangle$, which causes the atom to transfer to a ground state $|g_i\rangle$, while emitting a photon of the same frequency and in the same direction as the photon that caused the stimulated emission.

3. *Spontaneous emission* of a photon by an atom in an excited state $|e_i\rangle$, which causes the atom to transfer to a ground state $|g_j\rangle$, while emitting the photon in a random direction.

These processes are governed by the energy conservation equation $\Delta E_{ij} = h\nu_{ij}$, where h is Planck's constant and ΔE_{ij} is the energy difference between the states $|g_i\rangle$ and $|e_j\rangle$.

Spontaneous emission by an atom in state $|e_j\rangle$, that causes the atom to end up in state $|g_i\rangle$, is a natural process, that goes by rate γ_{ij} (note that the index of the ground state appears first).

On the other hand, stimulated absorption and stimulated emission between states $|g_i\rangle$ and $|e_j\rangle$ are caused by external fields, such as, in our case, the electromagnetic field of a laser. When the energy-levels are unperturbed, both of these processes go by a rate $\alpha_{ij}(\nu, \nu_{ij})I$, where I is the intensity and ν the frequency of the light to which the atoms are subjected. Here, $\alpha_{ij}(\nu, \nu_{ij})$ is given by

$$\alpha_{ij}(\nu, \nu_{ij}) = \alpha_{ij}^0 \mathcal{L}(\nu, \nu_{ij}) \tag{27}$$

with

$$\mathcal{L}(\nu, \nu_{ij}) = \frac{1}{1 + 4(\nu - \nu_{ij})^2/\gamma^2} \tag{28}$$

a Lorentzian distribution.

An important quantity of saturated absorption spectroscopy is the so called *saturation intensity*, defined by

$$I^{sat} = \frac{\gamma}{\alpha^0} \tag{29}$$

for $\alpha^0 = \max_{ij}\alpha_{ij}^0$ the strongest transition in the system. This is the intensity of the light for which the the atoms are equally likely to decay by stimulated emission or by spontaneous emission from the state $|e_j\rangle$ to the state $|g_i\rangle$ for which α_{ij}^0 is largest. For intensities much larger than I_{ij}^{sat}, the atoms are equally likely to be in state $|g_i\rangle$ or in $|e_j\rangle$.

3.1 Single-laser absorption spectroscopy - the two-level case

Saturated absorption spectroscopy is derived from an earlier version of laser spectroscopy where a single laser beam passes through a vapour cell. If the frequency of the laser corresponds to a transition frequency of the atoms, one may observe a change in absorption compared to off-resonant light, due to the stimulated absorption and emission processes. A crude two-level model may give some understanding of the corresponding physics. Let $|g_1\rangle$ and $|e_1\rangle$ be respectively the ground and the excited states of an atom. Then, conservation of energy implies:

$$I(x+dx) - I(x) = -h\nu\alpha_{11}(\nu,\nu_{11})I(x)(P_{g_1} - P_{e_1})n_0 dx \tag{30}$$

Here, we denoted the particle density by n_0 and the probability to find an atom in state $|s\rangle$ by P_s. Here, we neglect quantum coherences. One can thus define the *absorption coefficient* κ as

$$\kappa = h\nu\alpha_{11}(\nu,\nu_{11})I(x)(P_{g_1} - P_{e_1})n_0 \tag{31}$$

To understand saturated absorption spectroscopy, it is necessary to introduce the concept of *Doppler shifts*. Imagine an atom moving at velocity v in the same direction as the laser, which propagates with frequency ν. From the perspective of the atom, the the laser frequency will be shifted by an amount $\nu\frac{v}{c}$, where c is the speed of light. Therefore, the atom's resonant frequency becomes dependent of its velocity. To take this into account, we introduce the *Doppler shifted resonant frequency* between states $|g_i\rangle$ and $|e_j\rangle$:

$$\nu'_{ij} = \nu_{ij}(1 + \frac{v}{c}) \tag{32}$$

We observe that the resonant frequency is increased when the atom moves in the same direction as the laser beam, whereas the resonant frequency decreases when the atom moves in the opposite direction.

In order to add this Doppler shift to our model for the absorption, we now have to know the fraction of the atoms at velocity v. This is taken care of by substituting a Boltzmann velocity distribution $n(v)$ for n_0 in equation 30, given by

$$n(v) = n_0\sqrt{\frac{m}{2\pi k_B T}}e^{\frac{-mv^2}{2k_B T}} \tag{33}$$

where m is the atomic mass, T is the temperature and k_B is Boltzmann's constant. Next, we insert ν'_{ij} into equation 30 instead of ν_{ij} and then integrate over v. This yields

$$\kappa = \int_{-\infty}^{\infty} h\nu\alpha_{11}(\nu, \nu'_{11})I(x)(P_{g_1} - P_{e_1})n(v)dv \tag{34}$$

The final step towards our solution for the two-level model would then be to find some useful expression for $P_{g_1} - P_{e_1}$, the difference in probability to find an atom in state $|g_1\rangle$ and $|e_1\rangle$. Since the rate of change in both populations is determined by the previously described absorption and emission processes, we can give differential equations for $\frac{dP_{g_1}}{dt}$ and $\frac{dP_{e_1}}{dt}$, namely:

$$\begin{aligned} \frac{dP_{g_1}}{dt} &= \gamma_{11}P_{e_1} - \alpha_{11}(\nu, \nu'_{11})I(x)(P_{g_1} - P_{e_1}) \\ \frac{dP_{e_1}}{dt} &= -\gamma_{11}P_{e_1} + \alpha_{11}(\nu, \nu'_{11})I(x)(P_{g_1} - P_{e_1}). \end{aligned} \tag{35}$$

In addition, the axioms of probability imply that

$$P_{g_1} + P_{e_1} = 1. \tag{36}$$

Here, we neglected population changes due to particle collisions, because they occur in a much larger time frame than the changes due to stimulated absorption and emission. At first glance, the above equations seem to present us with an overdetermined system. Fortunately, the second equation can be obtained from the first and the third (by differentiating the latter) as can the first equation be obtained from the second and the third. In solving this system, we thus need only to use the third equation and either of the first two. If we demand $P_{g_1}(0) = 1$, which is a fair approximation, since $E_{g_1} \ll E_{e_1}$, we find

$$(P_{g_1} - P_{e_1})(t) = \frac{2I(x)\alpha_{11}(\nu, \nu'_{11})e^{-t(2\alpha_{11}(\nu,\nu'_{11})I(x)+\gamma_{11})} + \gamma_{11}}{2I(x)\alpha_{11}(\nu, \nu'_{11}) + \gamma_{11}} \tag{37}$$

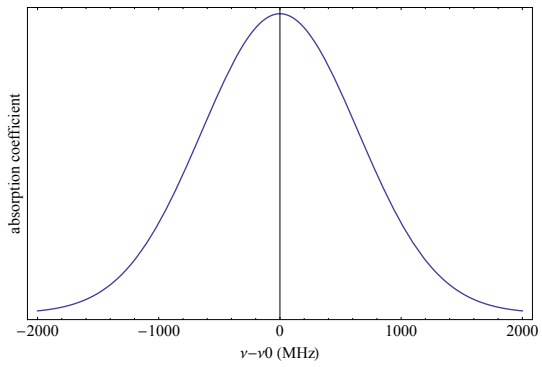

Figure 3.1: The absorption coefficient as a function of frequency for a typical sodium transition at $T = 400$.

In general, the spontaneous emission rate and the stimulated emission and absorption rates are very large, which mean that the system will equilibrate very fast. For most purposes, we can therefore neglect the exponential, so that we arrive at:

$$P_{g_1} - P_{e_1} = \frac{1}{1 + 2I(x)\alpha_{11}(\nu, \nu'_{11})/\gamma_{11}} \tag{38}$$

Now that we have found an expression for the population differences, we can plug our result into equation 34 to obtain the absorption spectrum for a two-level system. See figure 3.1 for a typical result of this calculation.

3.2 Single-laser absorption spectroscopy - the multi-level case

In reality, the ground and excited states of an atom are split due to effects such as hyperfine splitting. This means that the absorption signal may exhibit multiple peaks and asks for a generalisation of the formulae in the previous section to a more general system. Here, we will investigate the case where an atom has n ground levels and where the first excited state is divided into m sublevels.

We can therefore rewrite the absorption coefficient in equation 34 for this case as a sum over the different energy levels:

$$\kappa = \int_{-\infty}^{\infty} \sum_{i=1}^{n} \sum_{j=1}^{m} h\nu \alpha_{ij}(\nu, \nu'_{ij}) I(x)(P_{g_i} - P_{e_j}) n(v) dv \tag{39}$$

The next step is to obtain expressions for $(P_{g_i} - P_{e_j})$. We can do this by generalising equation 35 to the system of our interest. For the ground states, this yields:

$$\begin{aligned}
\frac{dP_{g_1}}{dt} &= \sum_{j=1}^{m} \Big(\gamma_{1j} P_{e_j} - \alpha_{1j}(\nu, \nu'_{1j}) I(x)(P_{g_1} - P_{e_j}) \Big) \\
\frac{dP_{g_2}}{dt} &= \sum_{j=1}^{m} \Big(\gamma_{2j} P_{e_j} - \alpha_{2j}(\nu, \nu'_{2j}) I(x)(P_{g_2} - P_{e_j}) \Big) \\
&\vdots \\
\frac{dP_{g_n}}{dt} &= \sum_{j=1}^{m} \Big(\gamma_{nj} P_{e_j} - \alpha_{nj}(\nu, \nu'_{nj}) I(x)(P_{g_n} - P_{e_j}) \Big)
\end{aligned} \tag{40}$$

While we obtain for the excited states:

$$\begin{aligned}
\frac{dP_{e_1}}{dt} &= \sum_{i=1}^{n} \Big(-\gamma_{i1} P_{e_1} + \alpha_{i1}(\nu, \nu'_{i1}) I(x)(P_{g_i} - P_{e_1}) \Big) \\
\frac{dP_{e_2}}{dt} &= \sum_{i=1}^{n} \Big(-\gamma_{i2} P_{e_2} + \alpha_{i2}(\nu, \nu'_{i2}) I(x)(P_{g_i} - P_{e_2}) \Big) \\
&\vdots \\
\frac{dP_{e_m}}{dt} &= \sum_{i=1}^{n} \Big(-\gamma_{im} P_{e_m} + \alpha_{im}(\nu, \nu'_{im}) I(x)(P_{g_i} - P_{e_m}) \Big)
\end{aligned}$$

And finally, we add the last ingredient to our equations:

$$\sum_{i=1}^{n} P_{g_i} + \sum_{j=1}^{m} P_{e_j} = 1$$

These are $n + m + 1$ equations for $n + m$ unknowns, so this system may again seem overdetermined. Furthermore, we can now no longer assume equilibrium in all cases: when the laser is set far off resonance, the net transfer rate to some ground state $|g_i\rangle$ may very well be twice as large as the net transfer rate to some other ground state $|g_k\rangle$, which would mean that $\frac{P_{g_i}}{P_{g_k}} = 2$. However, since the detuning is very large, both transfer rates are very low and it will take long for the system to reach equilibrium. For example, at $t = 0.001$ after the laser has been switched on, the populations of the ground state energy levels of a sodium atom are still within a margin of 1% identical to their starting values, if the laser is detuned 1 GHz from resonance and the intensity of the beam is equal to $10I_{sat}$. For a beam diameter in the order of mm and a thermal velocity in the order of 100 m/s, this means that an atom will not be affected by the laser long enough for it to be transferred to another ground state, an effect ignored by the assumption of equilibrium.

We thus need to solve the differential equations as presented in equation 40. This is taken care of by writing them in matrix form:

$$\frac{d}{dt}\begin{pmatrix} P_{g_1} \\ P_{g_2} \\ \vdots \\ P_{g_n} \\ P_{e_1} \\ P_{e_2} \\ \vdots \\ P_{e_m} \end{pmatrix} = \begin{pmatrix} A & B \\ C & D \end{pmatrix} \begin{pmatrix} P_{g_1} \\ P_{g_2} \\ \vdots \\ P_{g_n} \\ P_{e_1} \\ P_{e_2} \\ \vdots \\ P_{e_m} \end{pmatrix} \tag{41}$$

where

$$A = \begin{pmatrix} -\sum_{j=1}^{m} \alpha_{1j}(\nu, \nu'_{1j})I(x) & 0 & \cdots & 0 \\ 0 & -\sum_{j=1}^{m} \alpha_{2j}(\nu, \nu'_{2j})I(x) & & 0 \\ \vdots & & \ddots & \vdots \\ 0 & 0 & \cdots & -\sum_{j=1}^{m} \alpha_{nj}(\nu, \nu'_{nj})I(x) \end{pmatrix} \tag{42}$$

$$B = \begin{pmatrix} \gamma_{11} + \alpha_{11}(\nu, \nu'_{11})I(x) & \gamma_{12} + \alpha_{12}(\nu, \nu'_{12})I(x) & \cdots & \gamma_{1m} + \alpha_{1m}(\nu, \nu'_{1m})I(x) \\ \gamma_{21} + \alpha_{21}(\nu, \nu'_{21})I(x) & \gamma_{22} + \alpha_{22}(\nu, \nu'_{22})I(x) & \cdots & \gamma_{2m} + \alpha_{2m}(\nu, \nu'_{2m})I(x) \\ \vdots & \vdots & \ddots & \vdots \\ \gamma_{n1} + \alpha_{n1}(\nu, \nu'_{n1})I(x) & \gamma_{n2} + \alpha_{n2}(\nu, \nu'_{n2})I(x) & \cdots & \gamma_{nm} + \alpha_{nm}(\nu, \nu'_{nm})I(x) \end{pmatrix}$$

$$C = \begin{pmatrix} \alpha_{11}(\nu,\nu'_{11})I(x) & \alpha_{21}(\nu,\nu'_{21})I(x) & \cdots & \alpha_{n1}(\nu,\nu'_{n1})I(x) \\ \alpha_{12}(\nu,\nu'_{12})I(x) & \alpha_{22}(\nu,\nu'_{22})I(x) & \cdots & \alpha_{n2}(\nu,\nu'_{n2})I(x) \\ \vdots & \vdots & \ddots & \vdots \\ \alpha_{1m}(\nu,\nu'_{n1})I(x) & \alpha_{2m}(\nu,\nu'_{n2})I(x) & \cdots & \alpha_{nm}(\nu,\nu'_{nm})I(x) \end{pmatrix}$$

$$D = \begin{pmatrix} -\sum_{i=1}^{n}\left(\gamma_{i1} + \alpha_{i1}(\nu,\nu'_{i1})I(x)\right) & 0 & \cdots & 0 \\ 0 & -\sum_{i=1}^{n}\left(\gamma_{i2} + \alpha_{i2}(\nu,\nu'_{i2})I(x)\right) & & 0 \\ \vdots & & \ddots & \vdots \\ 0 & 0 & \cdots & -\sum_{i=1}^{n}\left(\gamma_{im} + \alpha_{im}(\nu,\nu'_{im})I(x)\right) \end{pmatrix}$$

In this case, the abundancy of equations is taken care of by choosing the starting conditions such that $\sum_{i=1}^{n} P_{g_i}(0) + \sum_{j=1}^{m} P_{e_j}(0) = 1$. If the energy levels of the excited states are sufficiently spaced from the energy of the ground state, we can neglect the population of the excited states, and set

$$P_{g_i}(0) = \frac{Eg_i/k_BT}{\sum_{k=1}^{n} E_{g_k}/k_BT} \tag{43}$$

and

$$P_{e_j} = 0 \tag{44}$$

for all $i = 1, 2, ..., n$ and $j = 1, 2, ..., m$. We then see that the solution for equation 40 is:

$$\begin{pmatrix} P_{g_1} \\ P_{g_2} \\ \vdots \\ P_{g_n} \\ P_{e_1} \\ P_{e_2} \\ \vdots \\ P_{e_m} \end{pmatrix} = \exp\left(\begin{pmatrix} A & B \\ C & D \end{pmatrix} t\right) \begin{pmatrix} P_{g_1}(0) \\ P_{g_2}(0) \\ \vdots \\ P_{g_n}(0) \\ 0 \\ 0 \\ \vdots \\ 0 \end{pmatrix}, \tag{45}$$

For the calculation of the exponent of a matrix, one can refer to Appendix A. For matrices of the rank that we typically encounter in problems of this kind, one can easily solve this equation for numerical values of the parameters.

However, upon further studying figure 3.1, we encounter a problem. Since the width of the peak in our spectrum is typically in the order of hundreds of MHz, whereas hyperfine splitting occurs at energy differences in the order of tens of MHz, we cannot distinguish between all the different levels. For that, we need a solution which comes by the name 'saturated absorption spectroscopy'.

3.3 Saturated absorption

The solution involves adding an extra laser beam to the setup, that propagates in the opposite direction with respect to the first laser at the same frequency ν. The original laser is called the *probe laser* and the new laser is called the *pump laser*. In an experiment, one measures the absorption of the probe laser. We assume that $I_{probe} \ll I_{sat} \ll I_{pump}$, which translates to the physical situation as the assumption that the change in the populations of the different energy levels in solely due to the pump laser.

Since both laser beams propagate in opposite directions, an atom with velocity v experiences opposite Doppler shifts with respect to both lasers. The transition frequency for the probe laser will remain $\nu'_{ij} = \nu_{ij}(1 + \frac{v}{c})$, but the transition frequency for the pump laser will become $\nu''_{ij} = \nu_{ij}(1 - \frac{v}{c})$.

We now investigate the absorption of the probe beam. If $\nu = \nu_{ij}$ for some transition from $|g_i\rangle$ to $|e_j\rangle$, only the atoms with zero velocity in the direction of the beams can absorb any of the probing light. However, since these atoms are also resonant with the pump beam, which has a much higher intensity, they are unlikely to be absorbed by the probe beam. This means one measures a dip in the absorption of the probe beam, compared to the situation where $\nu = \nu_{ij} + \Delta\nu_{ij}$ is detuned by a frequency difference of $\Delta\nu_{ij}$. This effect is called *hole burning*. Indeed, for in the situation where $\nu = \nu_{ij} + \Delta\nu_{ij}$, atoms with velocity equal to

$$v = -c\frac{\Delta\nu_{ij}}{\nu_{ij} + \Delta\nu_{ij}}$$

are resonant with the probe beam, while atoms with velocity equal to

$$v = c\frac{\Delta\nu_{ij}}{\nu_{ij} + \Delta\nu_{ij}}$$

are resonant with the pump beam. This means the absorption of the probe beam is not reduced by the transport of the atoms to other energy states by the pump beam, because both beams affect different velocity classes.

An interesting situation occurs when ν is set exactly between the transition frequencies of a single ground state to two different excited states (the *V-scheme*) or when it is set between the transition frequencies of two different ground states and a single excited state (the Λ-*scheme*). In the case of a V-scheme, the atoms that would normally be excited by the probe beam - that is, the atoms with velocity

$$v = \pm c\frac{\nu_{ij} - \nu_{il}}{\nu_{ij} + \nu_{il}}$$

(the $\pm$-sign occurs, because one velocity class is sent from state $|g_i\rangle$ to state $|e_j\rangle$, while the class with opposite velocity is sent from state $|g_i\rangle$ to state $|e_l\rangle$) - are now already excited by the pump beam. This shows up as a dip in the absorption.

In the case of a Λ-scheme, a somewhat similar situation occurs. We label the ground states by $|g_i\rangle$ and $|g_k\rangle$ and we label the excited state by $|e_j\rangle$. Normally, only atoms with velocity

$$v = c\frac{\nu_{ij} - \nu_{kj}}{\nu_{ij} + \nu_{kj}}$$

would be excited by the probe beam from ground state $|g_i\rangle$ to excited state $|e_j\rangle$, while the only atoms that would be excited from ground state $|g_k\rangle$ to $|e_j\rangle$ would have velocity

$$v = -c\frac{\nu_{ij} - \nu_{kj}}{\nu_{ij} + \nu_{kj}}.$$

However, now the atoms with velocity $v = -c\frac{\nu_{ij}-\nu_{kj}}{\nu_{ij}+\nu_{kj}}$ are excited by the pump beam from ground state $|g_i\rangle$ to excited state $|e_j\rangle$, because of the opposite sign in the Doppler shift and because the beam's frequency is set exactly between the two transition frequencies. These atoms can then decay to ground state $|g_k\rangle$, from where they can be excited again by the probe beam. The same story holds for the atoms with velocity $v = c\frac{\nu_{ij}-\nu_{kj}}{\nu_{ij}+\nu_{kj}}$ that are in ground state $|g_k\rangle$. We thus see a peak in the absorption, due to the larger fraction of atoms that can be excited by the probe beam than would normally be the case.

If we now want to calculate the absorption coefficient κ, we can again use the equation 39 and 45 for $\alpha_{ij}(\nu, \nu'_{ij})I_{probe}$, with the only difference that we should use $\alpha_{ij}(\nu, \nu''_{ij})I_{pump}$ in the equation for $P_{g_i} - P_{e_j}$, instead of $\alpha_{ij}(\nu, \nu'_{ij})I_{probe}$. In doing so, we assume that the population of the different states remains unaffected by the probe beam. This yields an absorption profile similar to 3.1, with the difference that we now see a dip when $\nu = \nu_{ij}$ or when $\nu = (\nu_{ij} + \nu_{il})/2$ and an extra peak when $\nu = (\nu_{ij} + \nu_{kj})/2$.

3.4 Calculating the saturated absorption spectrum of the D2-line in sodium

We know apply the theory set out in the previous sections to the D2-line in sodium. The spectrum is the result of transitions from a collection of eight ground states and sixteen excited states: the states that result from hyperfine splitting in the $3^2S_{1/2}$ ground state and from hyperfine splitting in the the $3^2P_{3/2}$ excited state. The ground states have total atomic angular momentum $F = 1$ and $F = 2$ and the excited states have total atomic angular momentum $F = 0$, $F = 1$, $F = 2$ and $F = 3$. Each state has sub-states that are generated by projection of F on the quantisation axis. This results in the quantum number $m_F = -F, -F + 1, ..., F$ that corresponds to the value of this projection.

3.4.1 Interaction with magnetic fields

In the absence of an electromagnetic field, a state with total atomic angular momentum F has $(2F+1)$-fold degeneracy, because the quantum number m_F does not contribute to the energy. However, the *Zeeman effect* caused by a magnetic field and the *Stark effect* caused by an electric field both break this degeneracy. Here, we shall confine ourselves

to the treatment of the Zeeman effect, following the course as set out by Steck in [11].

In the presence of a magnetic field in the z-direction, an extra term appears in the Hamiltonian of the atom, given by

$$H_B = \frac{\mu_B}{\hbar}(g_s\mathbf{S} + g_L\mathbf{L} + g_I\mathbf{I}) \cdot \mathbf{B} \tag{46}$$

$$= \frac{\mu_B}{\hbar}(g_s S_z + g_L L_z + g_I I_z)B_z, \tag{47}$$

where g_s, g_L and g_I are the the factors that denote the modifications in the dipole moments of the electron spin $\mathbf{S}$, electron orbital angular momentum $\mathbf{L}$ and nuclear spin $\mathbf{I}$ respectively and where μ_B is the Bohr magneton. The values of these constants can be found in [11].

For energy shifts caused by a magnetic field that are small when compared to the hyperfine splitting, the change in the energy levels can be described by the weak Zeeman effect:

$$\Delta E = \mu_B g_F m_F B_z, \tag{48}$$

where the hyperfine Landé g-factor is given by:

$$g_F \approx g_J \frac{F(F+1) - I(I+1) + J(J+1)}{2F(F+1)}, \tag{49}$$

with g_J the constant that modifies the dipole moment of the total electron angular momentum $\mathbf{J} = \mathbf{L} + \mathbf{S}$ (its value can, again, be found in [11]).

On the other hand, when the energy shifts caused by the magnetic field are large compared to the hyperfine splitting, the change in the energy levels can be described by the strong Zeeman effect:

$$\Delta E = \mu_B(g_J m_J + g_I m_I)B_z. \tag{50}$$

For determining the correct values of the quantum number, note that we have the following rules:

$$|L - S| \leq J \leq L + S \tag{51}$$

$$|J - I| \leq F \leq J + I \tag{52}$$

$$m_F = m_I + m_J. \tag{53}$$

Furthermore, for Sodium, $I = 3/2$, $J = 1/2$ in the ground states and $J = 3/2$ in the excited states of our interest.

3.4.2 Numerical simulations

Because the amount of terms in the solutions to equation 45 goes as $(m+n)!$, the length of the analytic solution in our case would be in the order of $24! \approx 10^{24}$. Since expressions

of this kind cannot be handled by the current computers, we have to resort to numerical methods.

In a typical saturated absorption experiment, the absorption is measured as a function of ν. We therefore have to perform the integration over the velocity in equation 39 for different values of ν. This is carried out within the approximation where we neglect the values of v for which $\alpha_{ij}(\nu, \nu'_{ij})$ is small (recall that ν'_{ij} depends on the velocity): we first select the exact velocity classes that are resonant with the probe beam and then define the set:

$$V = \{v : \exists i, j(\exists k \in \mathbb{Z}_m(v = v_{ij} \pm \Delta k))\}, \tag{54}$$

where v_{ij} is the velocity for which atoms in state $|g_i\rangle$ are excited by the probe beam to state $|e_j\rangle$, Δ defines the spacing between the different velocities for which we will be evaluating the integrand in equation 39 and m defines an upper and lower bound to V.

We then proceed by sorting V and deleting duplicates, such that it has the form $V = v_1, v_2, ..., v_p$ with $v_i < v_{i+1}$, so that we can take Riemann sums as follows:

$$\kappa \approx \sum_{k=1}^{p} \min(\Delta, \frac{v_{k+1} - v_{k-1}}{2}) \sum_{i=1}^{n} \sum_{j=1}^{m} h\nu\alpha_{ij}(\nu, \nu'_{ij}) I_{probe}(x)(P_{g_i} - P_{e_j})n(v), \tag{55}$$

where ν'_{ij}, P_{g_i} and P_{e_j} are evaluated in v_k and where the time-dependent solutions of P_{g_i} and P_{e_j} are evaluated at $t = 0.00005$. This time is chosen, because the diameter of the laser beam in the experiment to which we will be comparing our results is in the order of mm, while the thermal velocity of the atoms is in the order of 10^2 m/s. The values for α^0_{ij} and γ_{ij} are taken as stated in [12].The results of this calculation can be viewed in the figures 3.2 and 3.3.

3.5 Conclusion and discussion

From our results, we conclude that we can calculate the saturated absorption spectroscopy spectrum for sodium, using a semi-classical model. In the figures 3.2 and 3.3, we observe that our model allows us to predict the presence and the location of both the regular peaks and the cross-over signals, but our method appears to be of limited use when calculating the exact height and width of the peaks.This is at least partly due to our treatment of the pump beam: we neglected the Gaussian profile of its waist, assuming its intensity to be constant within some boundaries. If we were to fully incorporate this in our model, we would have to perform an addition integration over space to take into account the different laser light intensities to which the atom are subjected, blowing up our computation times, which are in the order of hours for the present model.

Also, in the case of a non-zero magnetic field, the errors seemed to be larger. This can be attributed to the limited accuracy that we could obtain when we determined the evaluation time for our solutions to equation 45.

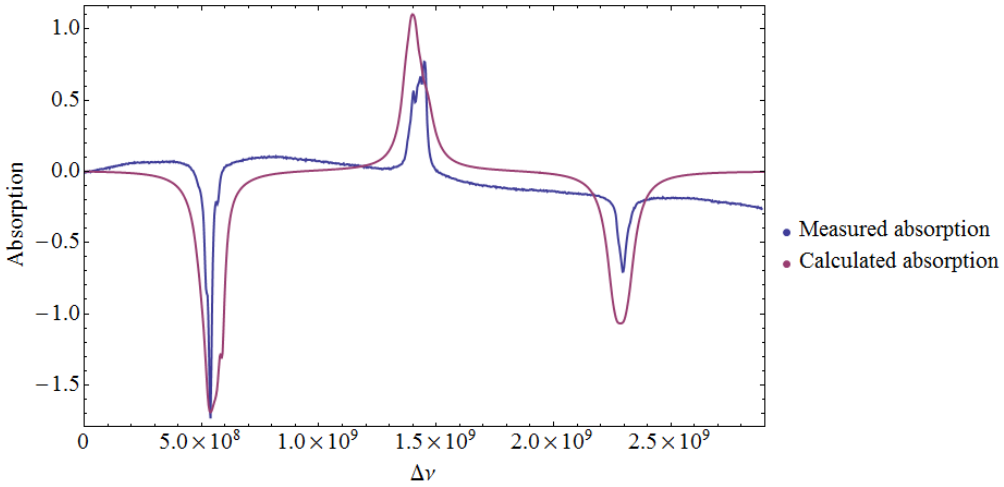

Figure 3.2: *The absorption profile as calculated and as measured at* $T = 406\ K$ *and* $n_0 = 4.7 \times 10^{16}$.

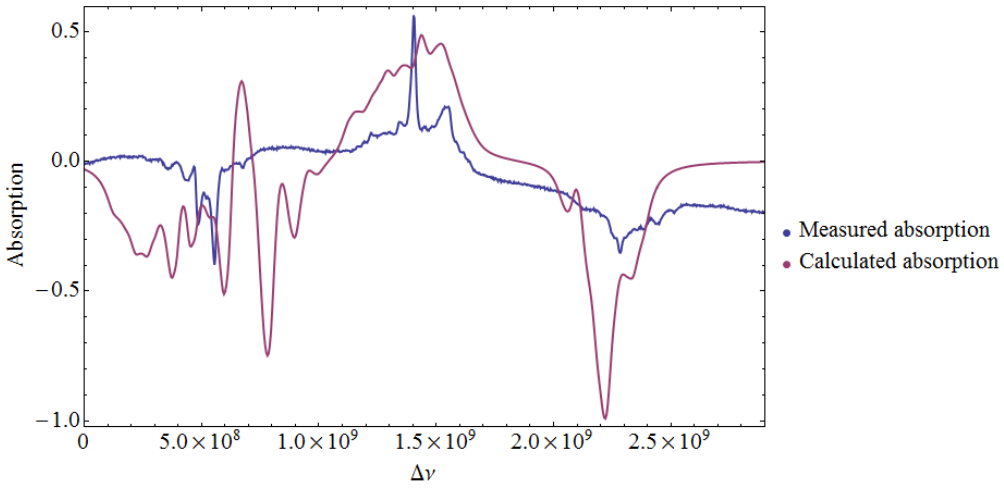

Figure 3.3: *The absorption profile as calculated and as measured at* $T = 406\ K$ *and* $n_0 = 4.7 \times 10^{16}$. *Here, we assumed a homogeneous magnetic field in the z-direction with magnitude* 68 *G. In the experiment, this field was generated by a solenoid with inner radius of* 25.5 *mm, outer radius of* 27 *mm, length* 9.8 *mm, current* 3 *A and approximately 200 windings,*

Furthermore, we should also integrate over the velocities of the atoms perpendicular to the direction of propagation of the beam: this would allow to get rid of the estimate of the correct evaluation time of our solutions to equation 45, instead calculating the exact exposure times of the different velocity classes to the laser beam. This has the same disadvantage as before, namely dramatically increasing our computation times.

As a final improvement, one could take into account quantum coherences between the different energy states. This was left out of our model, since it would increase its complexity, but it has the potential of leading to more accurate calculations.

4 Acknowledgements

During the process that led to this thesis, I have been fortunate enough to receive the support of a number of people. Here, I would like to take the opportunity to express my gratitude. First of all, I would like to thank Peter van der Straten, the head of the research group for his help when I got stuck and for introducing me to the topic of artificial gauge fields, which has been steadily garnering my interest during the year.

I would also like to thank Pieter Bons for his supervision on my work and I wish him the best during the last stages of his PhD research. Also, I am indebted to Stefan for the work he did on the topic of artificial gauge fields a year earlier, which has greatly helped me on my way.

Then, there are my fellow students, Rens, Thijs and Christian, that have made this time even more enjoyable for me. In particular, I thank Christian for all his help with the new fibre ports.

Lastly, I thank the technicians, namely Cees, Frits, Dante and Paul, for all their enthusiasm and helpfulness, whenever I needed their insight.

A The exponent of a matrix

Let M be a matrix of dimension d. Then the exponent of M is defined as:

$$\exp(M) = I + M + \frac{1}{2!}M^2 + \frac{1}{3!}M^3 + ... \tag{56}$$

In the case of zero degeneracy in the eigenvalues of M, we can simplify this expression: let λ_i and $\mathbf{v}_i$ be the eigenvalues and eigenvectors of M for $i = 1, 2, ..., d$, let Λ be given by

$$\Lambda = \begin{pmatrix} \lambda_1 & 0 & \cdots & 0 \\ 0 & \lambda_2 & & 0 \\ \vdots & & \ddots & \vdots \\ 0 & 0 & \cdots & \lambda_d \end{pmatrix} \tag{57}$$

and finally, let V be given by

$$V = \begin{pmatrix} \mathbf{v}_1 & \mathbf{v}_2 & \cdots & \mathbf{v}_d \end{pmatrix}. \tag{58}$$

Then, we know that

$$M = V\Lambda V^{-1}, \tag{59}$$

which gives, if we insert it in equation 56:

$$\exp(M) = I + V\Lambda V^{-1} + \frac{1}{2!}V\Lambda V^{-1}V\Lambda V^{-1} + \frac{1}{3!}V\Lambda V^{-1}V\Lambda V^{-1}V\Lambda V^{-1} \tag{60}$$

$$= V(I + \Lambda + \frac{1}{2!}\Lambda^2 + \frac{1}{3!}\Lambda^3)V^{-1} \tag{61}$$

$$= V \begin{pmatrix} \exp(\lambda_1) & 0 & \cdots & 0 \\ 0 & \exp(\lambda_2) & & 0 \\ \vdots & & \ddots & \vdots \\ 0 & 0 & \cdots & \exp(\lambda_d) \end{pmatrix} V^{-1} \tag{62}$$

Since it is straightforward to numerically calculate eigenvectors and eigenvalues of matrices, this formula allows one to calculate the exponent of large matrices.

References

[1] Chenau, M., Rath, S.P., Yefsah, T., Günter, K.J., Juzeliunas, G., and Dalibard, J. *Geometric Potentials in Quantum Optics: A Semi-Classical Interpretation* EPL **83**, 60001 (2008)

[2] Zhu, S.-L., H. Fu, C.-J. Wu, S.-C. Zhang, and L.-M. Duan *Spin Hall Effects for Cold Atoms in a Light-Induced Gauge Potential*, Phys. Rev. Lett. **97**, 240401 (2006)

[3] Korenberg, S., *Light-Induced Magnetic Fields for Neutral Atoms*, Bachelor's thesis, Universiteit Utrecht (2013)

[4] Dalibard, J., Gerbier, F., Juzeliunas, G. and Öhberg, P., *Articial gauge potentials for neutral atoms*, arXiv:1008.5378 [cond-mat.quant-gas] (2011)

[5] Duine, R.A. and Stoof, H.T.C, *Spin Drag in Noncondensed Bose Gases*, Phys. Rev. Lett. 103, 170401 (2009)

[6] Pethick, C. and Smith, H., *Bose-Einstein Condensation in Dilute Gases*, Cambridge University Press (2002)

[7] van 't Woud, M., *Spin drag below the condensation temperature of an ultra-cold Bose-gas*, Master's thesis, Universiteit Utrecht (2013)

[8] van Ooijen, E.D., *Realization and Illumination of Bose-condensed Sodium Atoms*, PhD thesis, Universiteit Utrecht, (2005)

[9] Wikipedia entry for "Elliptic integral", `http://en.wikipedia.org/wiki/Elliptic_integral`

[10] *Saturation Absorption Spectroscopy*, Manual, University of Florida, (2010)

[11] Steck, D. A., *Sodium d line data*, Online available at `http://steck.us/alkalidata` (revision2.0.1, 2 May 2008).

[12] Metcalf, J.M., and van der Straten, P., *Laser Cooling and Trapping*, Springer-Verlag, New York, (1999)